Astroparticle Physics 35 (2012) 573–590

Contents lists available at SciVerse ScienceDirect

Astroparticle Physics

journal homepage: www.elsevier.com/locate/astropart

The XENON100 dark matter experiment

E. Aprile[a], K. Arisaka[f], F. Arneodo[c], A. Askin[b], L. Baudis[b], A. Behrens[b], E. Brown[f], J.M.R. Cardoso[d], B. Choi[a], D. Cline[f], S. Fattori[c], A.D. Ferella[b], K.L. Giboni[a], A. Kish[b], C.W. Lam[f], R.F. Lang[a], K.E. Lim[a], J.A.M. Lopes[d], T. Marrodán Undagoitia[b], Y. Mei[e], A.J. Melgarejo Fernandez[a], K. Ni[a,1], U. Oberlack[e,2], S.E.A. Orrigo[d], E. Pantic[f], G. Plante[a], A.C.C. Ribeiro[d], R. Santorelli[a,b,3], J.M.F. dos Santos[d], M. Schumann[e,*,4], P. Shagin[e], A. Teymourian[f], E. Tziaferi[b], H. Wang[f], M. Yamashita[a,5], XENON100 Collaboration[6]

[a] *Department of Physics, Columbia University, New York, NY 10027, USA*
[b] *Physik-Institut, Universität Zürich, 8057 Zürich, Switzerland*
[c] *INFN – Laboratori Nazionali del Gran Sasso, 67010 Assergi, Italy*
[d] *Department of Physics, University of Coimbra, R. Larga, 3004-516 Coimbra, Portugal*
[e] *Department of Physics & Astronomy, Rice University, Houston, TX 77251, USA*
[f] *Department of Physics & Astronomy, University of California, Los Angeles, CA 90095, USA*

A R T I C L E I N F O

Article history:
Received 12 July 2011
Received in revised form 20 December 2011
Accepted 11 January 2012
Available online 21 January 2012

Keywords:
Dark matter
Direct detection
Liquid noble gas detector
XENON

A B S T R A C T

The XENON100 dark matter experiment uses liquid xenon (LXe) in a time projection chamber (TPC) to search for xenon nuclear recoils resulting from the scattering of dark matter Weakly Interacting Massive Particles (WIMPs). In this paper we present a detailed description of the detector design and present performance results, as established during the commissioning phase and during the first science runs.

The active target of XENON100 contains 62 kg of LXe, surrounded by an LXe veto of 99 kg, both instrumented with photomultiplier tubes (PMTs) operating inside the liquid or in xenon gas. The LXe target and veto are contained in a low-radioactivity stainless steel vessel, embedded in a passive radiation shield and is installed underground at the Laboratori Nazionali del Gran Sasso (LNGS), Italy. The experiment has recently published results from a 100 live-days dark matter search. The ultimate design goal of XENON100 is to achieve a spin-independent WIMP-nucleon scattering cross section sensitivity of $\sigma = 2 \times 10^{-45}$ cm^2 for a 100 GeV/c^2 WIMP.

1. Introduction

There is overwhelming observational evidence that about 23% of the matter and energy in the universe consists of cold dark matter [1–3], whose nature is still unknown and the subject of many investigations. Weakly Interacting Massive Particles (WIMPs) are a well-motivated class of dark matter candidates. WIMPs arise naturally in several models of physics beyond the Standard Model [2,4,5], for example in supersymmetric (SUSY) models where the lightest particles are among the most favored WIMP candidates [6,7]. They might be observed in terrestrial experiments, sensitive enough to measure the low-energy nuclear recoil resulting from the scattering of a WIMP with a nucleus [8].

The XENON dark matter project searches for nuclear recoils from WIMPs scattering off xenon nuclei. In a phased approach, experiments with increasingly larger mass and lower background are being operated underground, at the INFN Laboratori Nazionali del Gran Sasso (LNGS) in Italy [9], to probe WIMP-nucleon scattering cross-sections predicted by favored SUSY models [10]. The extraordinary sensitivity of XENON to dark matter is due to the combination of a large, homogeneous volume of ultra pure liquid xenon (LXe) as WIMP target, in a detector which measures not only the energy, but also the three spatial coordinates of each event occurring within the active target. Given the rapidly falling recoil energy spectrum from WIMP interactions, and the very low interaction cross sections predicted, the challenges for XENON, as for all direct detection experiments, are to achieve a very low radioactive background and energy threshold.

The XENON detectors are two-phase (liquid–gas) time projection chambers (TPCs), with simultaneous detection of the Xe scintillation light (S1) at the few keV$_{ee}$ level (keV electron equivalent

---

* Corresponding author.
E-mail addresses: age@astro.columbia.edu (E. Aprile), marc.schumann@physik.uzh.ch (M. Schumann).

[1] Present address: Department of Physics, Shanghai Jiao Tong University, China.
[2] Present address: Institut für Physik, Universität Mainz, Germany.
[3] Present address: CIEMAT, Madrid, Spain.
[4] Present address: Physik-Institut, Universität Zürich, Switzerland.
[5] Present address: Kamioka Observatory, ICRR, University of Tokyo, Japan.
[6] List includes XENON100 member institutions as of March 2009.

0927-6505/$ - see front matter © 2012 Elsevier B.V. All rights reserved.
doi:10.1016/j.astropartphys.2012.01.003

[11]), and ionization (S2) at the single electron level. For a recent review of the properties of LXe as scintillator and ionizer we refer to [12] and references therein. The ratio S2/S1 produced by a WIMP (or neutron) interaction is different from that produced by an electromagnetic interaction, allowing a rejection of the majority of the gamma and beta particle background with an efficiency around 99.5% at 50% nuclear recoil acceptance. The event localization with millimeter spatial resolution and the self-shielding capability of the LXe enable further background suppression by selection of a fiducial volume. To demonstrate the XENON detector concept, the R&D phase [11,13,15–17] culminated with a 10 kg scale TPC prototype (XENON10), operated at LNGS from 2006–2007 [18]. XENON10 achieved some of the best limits on WIMP dark matter reported to-date [19–22]. The ZEPLIN-II [23] and ZEPLIN-III [24] experiments, conceived before XENON10, also employ the two-phase LXe TPC principle. They differ, however, in many details especially in the light detection and the background level.

In order to increase the sensitivity to the WIMP-nucleon scattering cross section by more than one order of magnitude with respect to the state-of-the-art in 2007, a new TPC with a factor of 10 more mass and a factor of 100 less electromagnetic background was designed to fit inside the improved passive shield built at LNGS for XENON10. By focusing on the detector's performance, the goal of a fast realization of the new and improved XENON100 experiment was successfully achieved.

Initial results [25,26] from XENON100, obtained from only 11 days of data acquired during the commissioning period at the end of 2009, have demonstrated [27] a background rate which is indeed a factor 100 less than that of XENON10. This was accomplished by careful selection of all detector materials regarding intrinsic radioactivity [28], a xenon target with lower ^{85}Kr contamination, a novel detector design leaving only low radioactive components close to the target, and by improving the passive shield. Finally, XENON100 features an active LXe veto and allows for tighter fiducial volume cuts while still retaining a sizeable target mass. New parameter space has been excluded, competing with the limits on spin-independent WIMP-nucleon scattering cross section obtained from the full exposure of the CDMS-II experiment [29]. At the time of writing, XENON100 has set the most stringent limit for a very large range of WIMP masses [30], and is currently the only LXe TPC in operation with a sensitivity reach of 2×10^{-45} cm^2 at 100 GeV/c^2 within 2012, and with a realistic WIMP discovery potential.

In this paper, we describe the design of the XENON100 detector and associated systems, and present results on its performance as established in the commissioning phase which concluded with the data reported in [25]. Following a brief summary of the operating principle of the XENON two-phase TPC, the specific design choices and implementation in the XENON100 experiment are detailed in Section 3. Section 4 deals with raw data processing and basic-level data analysis, followed by results from calibration runs in Section 5. The paper closes with an outlook in Section 6.

2. Principle of the XENON two-phase TPC

A schematic of the XENON two-phase (liquid–gas) time projection chamber (TPC) is shown in Fig. 1. A particle interaction in the liquid xenon (LXe) produces direct scintillation photons and ionization electrons. An electric field is applied across the LXe volume with appropriate potentials on a series of electrodes, drifting ionization electrons away from the interaction site. Electrons which reach the liquid–gas interface are extracted into the Xe gas, where the process of proportional scintillation takes place [31–33]. Both the direct (S1) and the proportional (S2) scintillation light, with 178 nm wavelength, are detected by photomultiplier tubes (PMTs) with optimized response in the vacuum ultraviolet (VUV) regime.

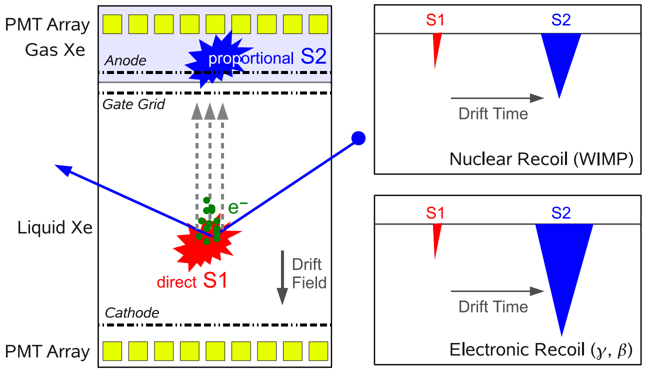

Fig. 1. (Left) Working principle of the XENON two-phase liquid–gas time projection chamber (TPC). See text for details. (Right) Sketch of the waveforms of two type of events. The different ratio of the charge (S2) and the light (S1) signal allows for the discrimination between nuclear recoils from WIMPs and neutrons and electronic recoils from gamma- and beta-background.

The electric field in the LXe volume is produced between a cathode at negative potential and a grounded gate grid, a few mm below the liquid–gas interface, see Fig. 1. A stronger electric field in the Xe gas above the liquid is produced between the gate grid and an anode grid placed a few mm above the liquid–gas interface. For a field larger than 10 kV/cm in the Xe gas, the electron extraction yield is close to 100% [13,14].

The time difference between the S1 and the S2 signals, caused by the finite electron drift velocity in LXe at the given drift field [12,34], is proportional to the *z*-coordinate (measured along the drift field direction) of the interaction vertex. The *x*- and *y*-coordinates can be inferred from the proportional scintillation hit pattern on the PMTs placed in the gas (top array). Thus, the XENON TPC provides full 3-dimensional vertex reconstruction on an event-by-event basis allowing for the fiducialization of the target to reduce radioactive backgrounds.

The different S2/S1 ratio of signals produced by electronic recoils (from gamma and beta background events) and by nuclear recoils (from WIMPs and neutrons) provides additional background discrimination [11,19]. The level of discrimination is found to be dependent on energy and electric field strength [17] and continues to be subject of experimental investigations.

3. The XENON100 experiment

The design goal of XENON100 was to increase the target mass by a factor of ten with respect to XENON10, and to achieve an electromagnetic background reduction of two orders of magnitude. In this section, we give a detailed description of the detector design and its realization, including all relevant sub-systems.

3.1. Detector design

The almost cylindrical XENON100 TPC of 30.5 cm height and of 15.3 cm radius contains the 62 kg LXe target (see Fig. 2). The walls delineating the cylindrical volume and separating it from an active LXe veto shield, which is surrounding the target, are made of 24 panels of 1/4 inch-thick polytetrafluorethylen (PTFE, Teflon). PTFE is chosen for its properties both as insulator and good reflector for the VUV scintillation light [35]. When cooled down to the LXe temperature of −91 °C, the PTFE panels shrink by about 1.5%. To avoid scintillation light to leak from the active target volume to the shield region, the panels are made interlocking. The TPC is closed on the bottom by the cathode, and on the top by the gate grid (see Section 3.2).

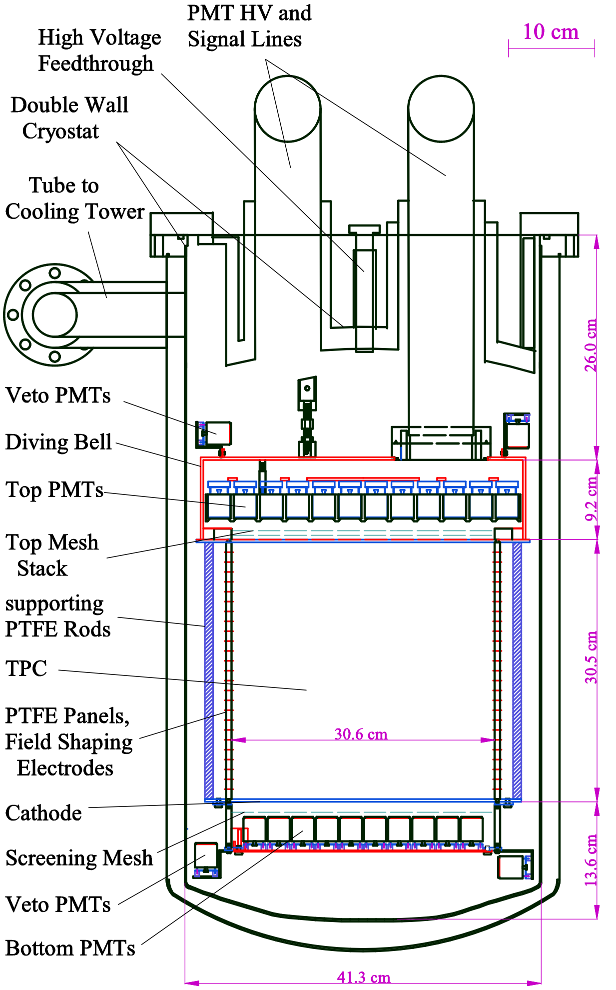

Fig. 2. Drawing of the XENON100 dark matter detector: the inner TPC contains 62 kg of liquid xenon as target and is surrounded on all sides by an active liquid xenon veto of 99 kg. The diving bell assembly allows for keeping the liquid–gas interface at a precise level, while enabling to fill LXe in the vessel to a height above the bell.

The two-phase (liquid–gas) operation requires a precisely controlled liquid level just covering the gate grid. To minimize the impact of liquid density variations due to temperature changes as well as fluctuations in the gas recirculation rate, a diving bell design was chosen to keep the liquid at a precise level. Outside the bell, the liquid in the detector vessel can be at an arbitrarily high level. This made it possible to fill the vessel to a height of about 4 cm above the bell, enabling a 4π coverage of the TPC with a LXe veto.

The bell keeps the liquid level at the desired height when a constant stream of gas pressurizes it. This is accomplished by feeding the xenon gas returning from the gas recirculation system (see Section 3.5) into the bell. The pressure is released through a small pipe that reaches out into the veto LXe volume. The height of the LXe level inside the bell is adjusted by vertically moving the open end of the pipe which is connected to a motion feedthrough.

In order to minimize the dependence of the charge signal on the *xy*-position, the liquid–gas interface has to be parallel to the anode. To facilitate leveling, the detector can be tilted with two set screws from the outside of the radiation shield. Four level meters, measuring the capacitance between partially LXe filled stainless steel tubes and a Cu rod placed in their center, as well as the measured S2 signal width at different locations, are used to level the detector (see Section 5.2).

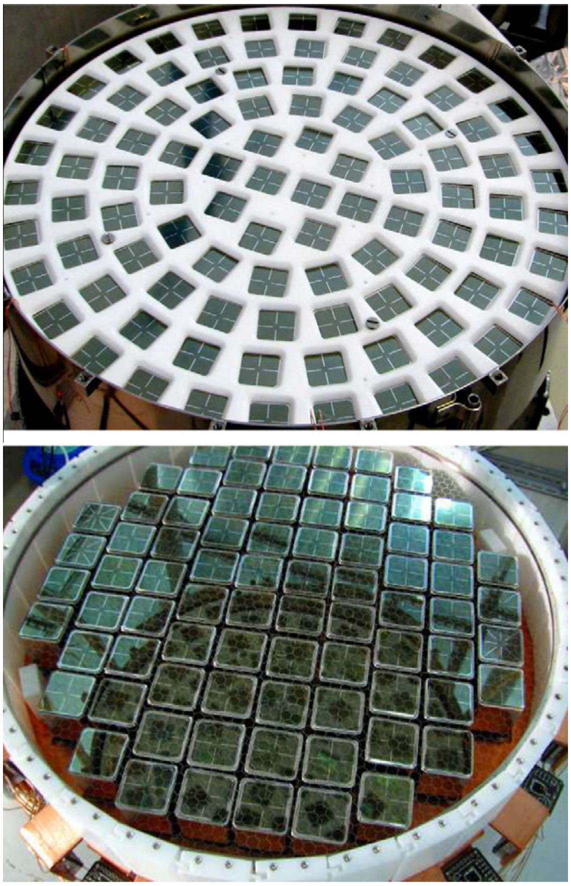

Fig. 3. (Top) The Hamamatsu R8520-06-Al PMTs on the top of XENON100 are arranged in concentric circles in order to improve the reconstruction of the radial event position. (Bottom) On the bottom, the PMTs are arranged as closely as possible in order to achieve high light collection, as required for a low detector threshold.

Two arrays of Hamamatsu R8520-06-Al 1” square photomultiplier tubes (PMTs), specially selected for low radioactivity [28], detect the light in the TPC: 98 PMTs are located above the target in the gas phase, arranged in concentric circles in order to improve the resolution of radial event position reconstruction, see Fig. 3 (top). The outmost ring extends beyond the TPC radius to improve position reconstruction at the edges. The remaining photocathode coverage is 43.9% of the TPC cross section area. The energy threshold and hence the sensitivity of the detector is determined by the S1 signal. Because of the large refractive index of LXe of (1.69 ± 0.02) [36], and the consequent total internal reflection at the liquid–gas interface, about 80% of the S1 signal is seen by the second PMT array, which is located below the cathode, immersed in the LXe. Here, 80 PMTs provide optimal area coverage (in average 52% useful PMT photocathode coverage with 61% in the central part) for efficient S1 light collection, see Fig. 3 (bottom). The bottom PMTs have a higher quantum efficiency compared to the top PMTs. This is shown in Fig. 4, together with the distribution of the PMT quantum efficiency in the detector. The photoelectron collection efficiency from the photocathode to the first dynode for this type of PMT is about 70%, according to Hamamatsu.

A LXe layer of about 4 cm thickness surrounds the TPC on all sides and is observed by 64 PMTs, of the same type as used for the TPC readout. In total, this volume contains 99 kg of LXe. The presence of this LXe veto, operated in anti-coincidence mode, is very effective for background reduction [27] and is one major difference in design compared to XENON10. The LXe veto is optically separated from the TPC by the interlocking PTFE panels. Optical

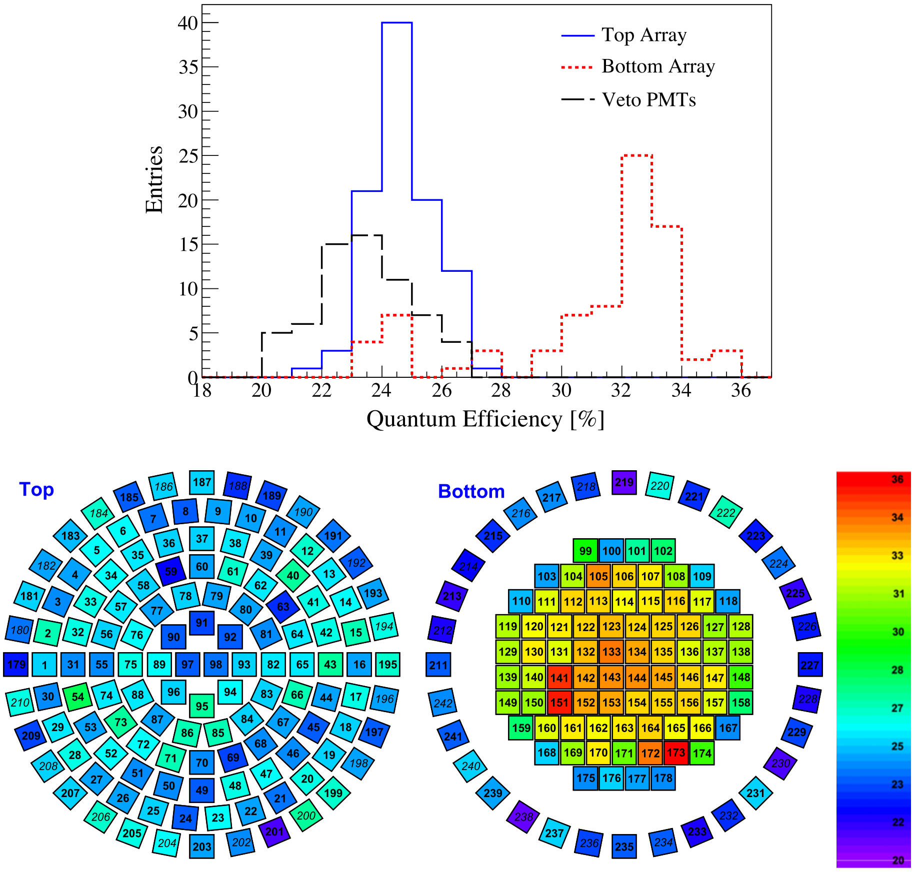

Fig. 4. (Top) Quantum efficiency (QE) distribution of the R8520–06-Al PMTs in XENON100, estimated at room temperature by Hamamatsu. The PMTs on the bottom have higher values to improve the energy threshold. (Bottom) Arrangement of the PMT with different QE (given by the color code) in the detector. Tubes with lower QE are placed mainly on the top, in the active veto or in detector corners, where they have less impact on the detector threshold.

separation of target and veto has some advantages over instrumenting the entire volume as TPC as it lowers the event rate in the target and reduces the rate of accidental coincidences to a negligible level. It also requires fewer PMTs and reduces cost.

The voltage divider, directly coupled to the PMT, is a printed circuit with surface mount components on a Cirlex substrate [37]. Compared to XENON10 [18], the design was modified and the number of electronic components was reduced in order to decrease the background contribution [28]. Each PMT is connected with a PTFE insulated coaxial cable to read the signal as well as a Kapton insulated single wire cable to supply the operating voltage. The outer insulation of the coaxial cable was removed to prevent potential impact of trapped air on LXe purity. This choice resulted in a common ground for all PMTs. The cables of the top PMTs are guided out of the passive shield through a pipe connecting to the bell. All other cables are grouped into four bunches which are fixed to the PTFE support structure, and guided on top of the bell where they are collected and routed out of the shield through a second pipe (see Fig. 2). Each pipe is equipped with commercial 48-pin vacuum feedthroughs at the end providing the connection to atmosphere, outside of the shielding.

Nine out of the 242 PMTs installed in XENON100 were not working during the physics run reported in [30]. Of these, four are on the top array (PMT 9, 12, 39, and 58), two on the bottom (PMT 100, 105) and three in the active veto (PMT 195, 224, 235). Three additional PMTs (148, 177, 191) were powered off due to high dark current. Overall, only 5% of the PMTs are non-functional at the time of writing, almost 3 years after the last detector opening for maintenance.

The TPC is mounted in a double-walled 316Ti stainless steel cryostat, selected for its low activity, especially in ^{60}Co [28]. Since the radioactive contamination of the cryogenics system, ceramic feedthroughs, etc. cannot be lowered easily, the detector is cooled remotely and all parts with a known high radioactive contamination are installed away from the detector itself, outside the passive shield (see Section 3.3 and Fig. 5). The connection to the outside of the shield is established via three stainless steel pipes, one double-walled to the cooling system, the others single-walled to the PMT feedthroughs and pumping ports. To bias the cathode and the anode, custom-made hermetic HV feedthroughs, of similar design as developed for XENON10 [18], are used also for XENON100. They are made of a stainless steel core with a PTFE insulation layer, for reduced radioactive contamination compared to commercial HV feedthroughs.

PTFE has a rather large linear thermal expansion coefficient $A \sim 1.2 \times 10^{-4}\,\mathrm{K}^{-1}$, as measured for the PTFE used in XENON100. This leads to a TPC contraction of ~5 mm when cooled to LXe temperatures. The contraction along the z-dimension is taken into account when the z-coordinate of an event is determined. Radial contraction is negligible since the PTFE panels are mounted between copper support rings which have a much smaller thermal expansion coefficient ($A_{Cu} \sim 1.5 \times 10^{-5}\,\mathrm{K}^{-1}$).

3.2. Electric field configuration

Thin metal meshes are used to create the electric fields required to operate XENON100 as a two-phase TPC. They were chemically etched from stainless steel foils and spot-welded onto rings made

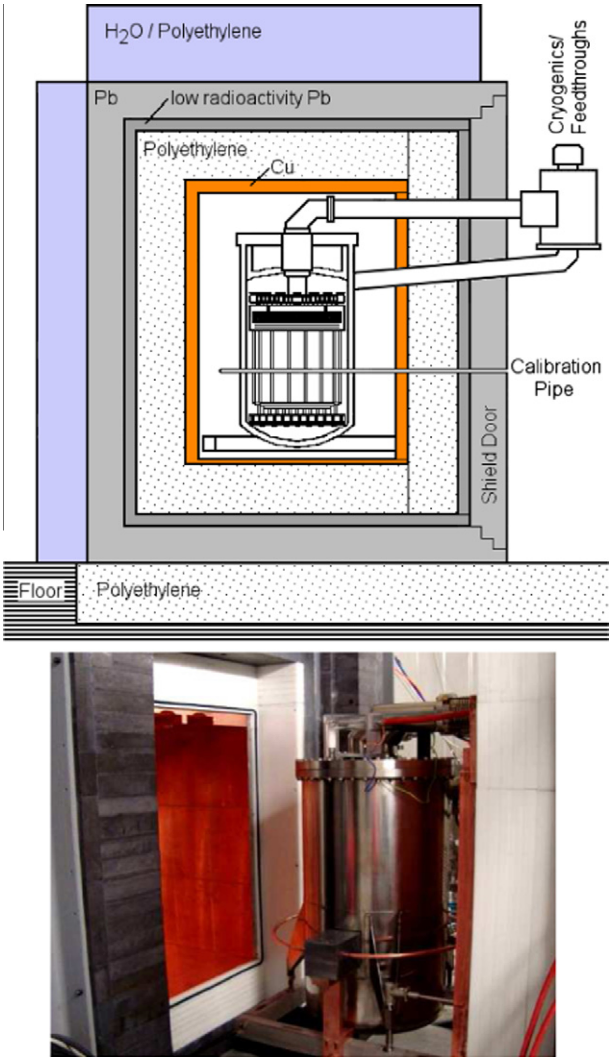

Fig. 5. (Top) Drawing of the XENON100 detector in its passive shield made out of copper, polyethylene, lead, and water containers. (Bottom) XENON100 with opened shield door. The Pb-brick along the calibration pipe around the cryostat is a gamma-shield during ^{241}AmBe neutron calibrations.

of the same low radioactivity stainless steel that is used for the cryostat. Before welding, the meshes were stretched in order to minimize sagging.

The cathode mesh is 75 μm thick with a hexagonal pattern and a pitch of 5 mm. A grounded screening mesh, also of hexagonal pattern and 5 mm pitch, but 50 μm thick, is placed 12 mm below the cathode, and 5 mm above the bottom PMTs to shield them from the cathode high voltage. According to the initial design, a voltage of −30 kV would bias the cathode, to generate a drift field of 1 kV/cm corresponding to a maximal electron drift time of ~160 μs. However, due to the appearance of small light pulses at increasingly high cathode voltage, the voltage was reduced to −16 kV for stable operation, resulting in a drift field of 0.53 kV/cm across the TPC. The pulses are most likely caused by electron field emission and subsequent scintillation in the strong electric field near sharp features of the cathode mesh.

The unavoidable liquid layer between the cathode and the bottom PMTs is a charge insensitive region and a potential source of events which can be confused with true nuclear recoils. For example, a background gamma-ray with two interactions, one in this insensitive region and one inside the TPC active region, may result in a reduced S2/S1 ratio, mimicking a nuclear recoil event (see e.g. [18,19]). These events mainly occur close to the cathode and can be reduced by a *z*-cut. In addition, the distribution of the S1 light on the PMTs differs from real single scatter interactions and this is exploited in data analysis [18,30].

About 15 mm below the top PMTs, the TPC is closed with a stack of three stainless steel meshes with hexagonal pattern: a central anode (125 μm thick, 2.5 mm pitch) between two grounded meshes with a spacing of 5 mm. An extraction field of ~12 kV/cm is obtained by applying +4.5 kV to the anode. The exact value of the extraction field depends on the position of the liquid–gas interface because of the different dielectric constants of LXe and Xe gas. The field is high enough to obtain an extraction efficiency close to 100% [13,14]. The grounded mesh above the anode shields the amplification region from external fields and yields more homogeneous proportional scintillation signals.

In order to optimize the S2 performance, the anode could be moved horizontally with respect to the gate grid and the top grid. It was aligned at a half-pitch offset under a microscope and fixed with set screws. The whole stack is optimized for optical transparency and minimal impact on the S2 energy resolution. The spread of the S2 signal due to the varying electron path length is only 4%, independent of the S2 energy. Averaged over all angles of incidence, the optical transparency of the top mesh stack and of cathode plus screening mesh is 47.7% and 83.4%, respectively.

A homogeneous electric field across the ~30 cm long TPC drift gap is created by a field cage structure made of thin copper wires. Two wires, at the same potential, one running on the inside and one on the outside of the PTFE panels, are used to emulate a 1/4 in.-wide field shaping electrode which generates the desired straight field lines within the target volume. Forty equidistant field shaping electrodes, connected through 700 MΩ resistors are used.

The penetration of electric field lines through the cathode, facilitated by the large mesh pitch and the thin wire diameter chosen to optimize light collection, distorts the electric field at large radii, just above the cathode. The correction of this effect, based on calibration data, is presented in Section 5.5.

3.3. The passive shield

The XENON100 experiment is installed underground at LNGS, at the same site as XENON10, in the interferometer tunnel away from the main experimental halls. At the depth of 3700 m water equivalent, the surface muon flux is reduced by a factor 10^6 [38].

In order to reduce the background from the radioactivity in the experiment's environment, in the laboratory walls, etc. [39], additional passive shielding is needed. An improved version of the XENON10 shield [18] was required in light of the increased sensitivity of the XENON100 experiment. The detector is surrounded (from inside to outside) by 5 cm of OFHC copper, followed by 20 cm of polyethylene, and 20 cm of lead, where the innermost 5 cm consist of lead with a low ^{210}Pb contamination of (26 ± 6) Bq/kg [28]. The entire shield rests on a 25 cm thick slab of polyethylene. An additional outer layer of 20 cm of water or polyethylene has been added on top and on three sides of the shield to reduce the neutron background further. Fig. 5 shows a sketch of XENON100 inside the shield.

During detector operation, the inner shield cavity is constantly purged with high purity boil-off nitrogen at a rate of 17 standard liters per minute (SLPM) in order to avoid radioactive radon penetrating into the shield. The remaining radon concentration is constantly monitored with a commercial radon detector and is at the limit of the detector's sensitivity (<1 Bq/m^3).

Careful selection of materials to build the detector is crucial in order to reach a competitive dark matter detection sensitivity. All components used for the XENON100 detector and shield have been chosen according to their measured low intrinsic radioactivity.

These measurements were performed using a dedicated screening facility [40], consisting of a 2.2 kg high purity Ge detector in an ultra-low background Cu cryostat and Cu/Pb shield, operated at LNGS, as well as the LNGS screening facilities [41,42].

The electronic recoil background of XENON100 is dominated by gamma rays from the decay chains of radioactive contaminants, mostly ^{238}U, ^{232}Th, ^{40}K, and ^{60}Co, in the detector materials. The screening results [28] are used to predict the overall background rate. Rate and spectral shape agree very well with the measurement [27].

3.4. Cryogenic system

A reliable, easy to use cooling system with very good stability is needed for any dark matter experiment operated at cryogenic temperatures. Pulse tube refrigerators (PTRs) [43], specifically designed for high cooling power at LXe temperatures, were employed from the start of the XENON project. The PTR for XENON100 is an Iwatani PC150, driven by a 6.5 kW helium compressor. The cooling power for this combination is measured to be 200 W at 170 K. A schematic of the cooling system is shown in Fig. 6.

The PTR cold-head is mounted on a cylindrical copper block that closes off the inner detector vessel and that acts as a cold-finger. The cold-finger is sealed to the inner detector vessel with a seal made of a pure aluminum wire. The PTR can thus be serviced or replaced without exposing the detector volume to air. A copper cup with electrical heaters is inserted between the PTR cold-head and the cold-finger. The temperatures above and below the heater are measured with precise temperature sensors. A proportional-integral-derivative (PID) controller regulates the heating power required to keep the temperature of the cold-finger, and hence the Xe vapor pressure in the detector, at the desired value.

The PTR is mounted in a separate double-walled vacuum insulated vessel, placed outside the passive shield, along with many auxiliary modules, including the motor valve and buffer tank, which have to be within 50 cm of the PTR cold-finger for optimal performance (see Fig. 6). The bottom of this "cooling tower" is connected to the main cryostat with a vacuum insulated pipe at a height above the liquid level. The boil-off Xe gas from the detector can thus reach the cold-finger of the PTR where it is liquefied. The liquid drops are collected by a funnel and flow back into the detector through a smaller diameter pipe at the center of the insulated pipe. To drive the liquid flow, the insulated pipe is inclined by 5° with respect to the horizontal. This cryogenic system design with the PTR assembly placed far from the detector, enabled a reduction of the background from radioactive materials [27]. The total mass of steel within the shield cavity was reduced from 180 kg for the much smaller XENON10 detector to about 70 kg for XENON100.

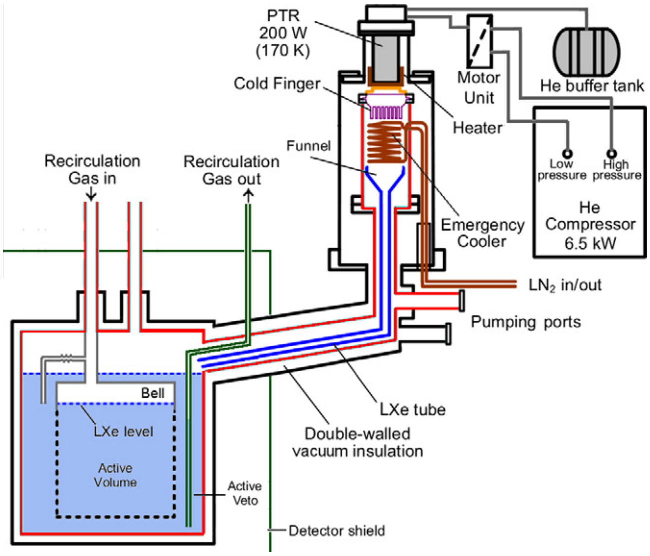

Fig. 6. Sketch of the XENON100 cryogenic system. The cooling is provided by a 200 W pulse tube refrigerator (PTR) installed outside the shield and connected to the main cryostat via a double-walled vacuum insulated pipe. Xenon purification is independent of the cooling. LXe is extracted from the bottom of the detector, purified in gas phase, and introduced back as xenon gas into the diving bell. In combination with a height-adjustable gas outlet pipe, the bell allows for a precise control of the liquid level, while having LXe all around the detector. The figure is not drawn to scale and details of the TPC are omitted for clarity.

In case of emergency, e.g., a prolonged power failure or a failure of the primary cooling system, the detector can be cooled by liquid nitrogen (LN$_2$). A stainless steel coil is wound around the cold finger and is connected to an external LN$_2$ dewar, always kept full during detector operation. The LN$_2$ flow through the coil is controlled by an actuated valve and triggered when the detector pressure increases above a defined set-point. Tests have shown that the detector can be kept stable for more than 24 h without any human intervention using the emergency LN$_2$ cooling system.

3.5. The gas handling and purification system

A total amount of 161 kg of LXe is necessary to fill the target volume and the active veto. It is stored in four large (75 l volume) high-pressure aluminum gas cylinders, which are surrounded by custom-made insulated LN$_2$ dewars. This allows them to be cooled down to recover the xenon gas from the detector by freezing the Xe in the cylinders. Both Xe filling and recovery takes place in gas phase, through a stainless steel pipe connecting the storage with the purification system (see below). All pipes, flow controllers, regulators, and valves are metal sealed. During the process of filling, the gas is liquefied by the PTR, which has sufficient cooling power to cool the vessel, condense the gas, and keep it at the operating temperature of −91°C. The xenon gas is liquefied at a rate of almost 3 kg/h, limited by the cooling capacity of the PTR.

During gas recovery, the Xe is extracted from the detector by a double-diaphragm pump and transferred to the storage cylinders at LN$_2$ temperature. Recovery is facilitated by breaking the vacuum insulation of the cryostat.

During the Xe purification from Kr, through a dedicated cryogenic distillation column (see Section 3.7), the gas stored in the cylinders is passed through the distillation column before being filled directly into the detector. To replenish the Kr-rich Xe, which is produced as "off-gas" during distillation, more Xe than needed for a complete fill of XENON100 is stored in the cylinders.

The light and the charge signal from particle interactions in the xenon are adversely affected by impurities in LXe: The light is mostly attenuated by water [44], whereas for the charge the most abundant and harmful impurity is oxygen which leads to charge losses while the electron cloud drifts towards the liquid–gas interface [45]. Hence, oxygen and other electro-negative impurities in commercial xenon have to be removed well below the 1 ppb (part per billion) level oxygen-equivalent to achieve the required low charge attenuation (high electron lifetime) and long VUV photon absorption length [12]. The xenon is purified by constantly recirculating xenon gas through a high temperature zirconium getter (*SAES MonoTorr PS3-MT3-R/N-1/2*, see Fig. 7), which removes impurities by chemically bonding them to the getter material. At a rate of about 5 SLPM, liquid from the bottom of the detector vessel is evaporated and pushed through the getter by a double diaphragm pump (*KNF N143.12E*), before it is returned to the detector.

In order to speed up the purification process already before filling with LXe, the leak-tested detector was heated to 50 °C (the temperature limit is set by the PMTs) while the detector vacuum

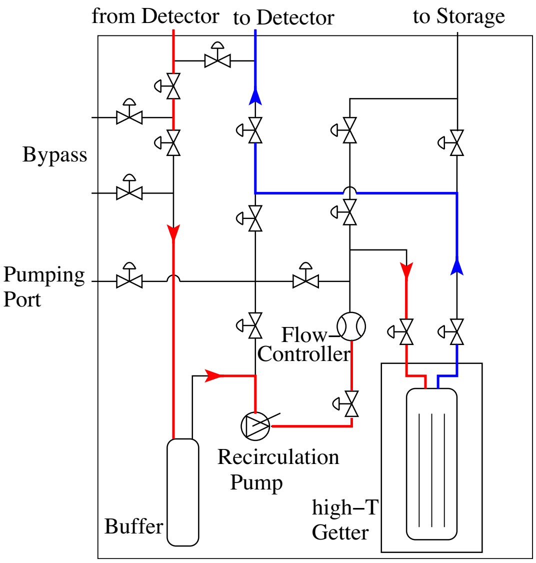

Fig. 7. Schematic of the XENON100 purification system. LXe is extracted from the detector using a diaphragm gas pump. It evaporates in the gas lines and is passed through a high temperature getter for gas purification, before it is pushed back into the detector (the path for standard operation is indicated by the arrows). Different valves allow for the bypassing of components for special operations like detector filling or recuperation, or maintenance. Valves to atmosphere are used to add auxiliary equipment for gas analysis or detector calibration.

was monitored with a residual gas analyzer (RGA). Since Xe is known to act as an effective solvent due to its polarizability [46], the detector was then filled with 2 atm of Xe gas. The detector was heated again while the warm gas was passed through the getter for purification for several weeks. During this process, the decrease of the water content from ~500 ppb to the 1 ppb level was monitored with a dedicated apparatus (*Tigeroptics HALO*) using a spectral absorption technique.

3.6. Light and charge yield evolution

Analyses of the light yield and the *z*-dependent charge yield from standard gamma calibration sources such as the 662 keV line from ^{137}Cs give access to the water and oxygen content in the LXe, respectively. During the initial commissioning phase of XENON100, the light yield of the LXe filled detector increased while water contamination, from materials outgassing, was reduced by continuous circulation of the gas through the high temperature getter (see Fig. 8). The time to reach the maximum light yield was considerably decreased between the runs. The detector was always exposed to atmosphere in between these runs, however, the detector preparation prior to filling the gas was improved, mostly by recirculation of Xe gas at a temperature of 50 °C for 2–3 weeks as described in Section 3.5, in order to clean the inner detector surfaces efficiently.

The pipes guiding all signal and HV cables out of the passive shield were designed to be single-walled to reduce the mass of possibly radioactive materials close to the detector. Consequently, their inner surfaces have temperatures of 5–20 °C during normal operation and thus exhibit a much higher outgassing rate than the surfaces at LXe temperature. This effect is additionally boosted by the large amount of wires (PTFE insulated coaxial wires for the signal and Kapton wires for the high voltage) in the pipes, constituting a large surface. Bake-out at the maximum allowed temperature (~ 120°C) and the continuous circulation of Xe gas reduced the outgassing with time, leading to a constant light yield during the XENON100 commissioning run [25] and the science run [30].

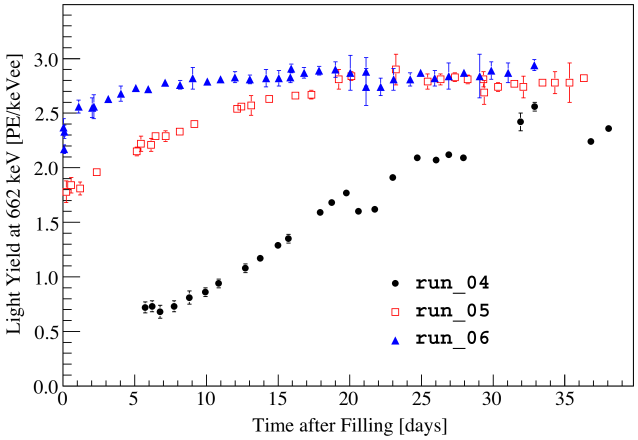

Fig. 8. Improvement of the light yield vs. time with continuous circulation through the getter, for several early commissioning runs. The yield, corresponding to the value of the 662 keV full-absorption peak, was measured with an external ^{137}Cs source at zero drift field and no position dependent corrections have been applied to the data. The maximum was reached in all cases but on different timescales due to different and improved preparation of the detector.

The charge yield in LXe, at a given drift field, is strongly affected by electronegative impurities dissolved in the liquid. External leaks, surface outgassing, and contaminations present in the liquid itself all may contribute. The remaining amount of electronegative impurities must be kept at the sub-ppb level of O_2 equivalent in order to drift freely ionization electrons across large distances. With about 30 cm, the drift gap in the XENON100 TPC is twice as long as that of XENON10 and the longest of any ionization detector operating with LXe to-date. The stringent constraints on materials choice driven by radio-purity, the limited allowed temperature range of the PMTs and their voltage-divider network, the large amount of cabling, the limited speed in gas purification rate determined by the total available cooling power, all contributed to the challenge of achieving long electron drift in this novel detector. Compared to the time required to reach the maximal scintillation light yield, it took much longer to achieve a LXe purity which allowed for electrons to drift over the full 30 cm gap. This was largely due to the dominating role of materials outgassing and due to impurities introduced by leaks of the vessel which developed during transport and installation underground.

The electron lifetime $\tau_e = (k_n n)^{-1}$, where k_n is the attachment rate coefficient, is a measure of the number of electrons lost during the drift time, and thus a measure of the total impurity concentration n in the liquid. In the XENON100 TPC, this number is regularly monitored by measuring the S2 signal of the full-absorption peak of 662 keV gamma-rays in the fiducial volume as a function of drift time, using an external ^{137}Cs source. The evolution of τ_e with purification time, shown in Fig. 9 for the published science runs [25,30], indicates that the maximum has yet to be reached, leading to a time-dependent correction to the data. During dark matter data taking, this charge calibration is done regularly in order to correct the S2 signal for charge loss, using linear interpolation between calibrations or a linear fit (see Section 5.3). At the time of writing, values larger than 550 µs have been achieved (see Fig. 19) and the maximum has not been reached yet.

3.7. The Krypton distillation system

Xenon has no long-lived radioactive isotopes and the half-life of the potential double-beta emitter ^{136}Xe is so long [47] that it does not limit the sensitivity of current LXe detectors. As a condensed noble gas, Xe is readily purified from most radioactive impurities

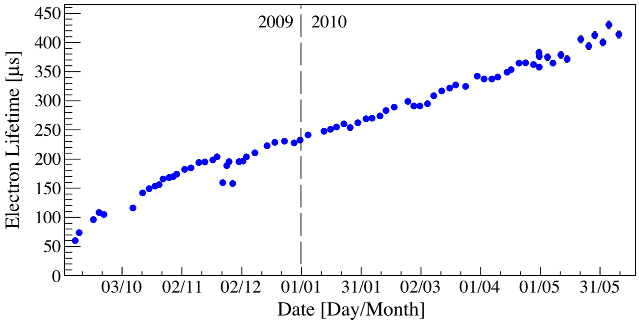

Fig. 9. Evolution of the electron lifetime τ_e, measured with a ^{137}Cs source, during the commissioning run [25] and the first science run [30] which started on January 13, 2010. The decrease around the end of November 2009 is due to a stop of xenon purification during an exchange of the recirculation pump. In the meantime, values of $\tau_e > 0.5$ ms have been achieved.

with one notable exception: ^{85}Kr, with an isotopic abundance of $^{85}\mathrm{Kr}/^{\mathrm{nat}}\mathrm{Kr} \sim 10^{-11}$ [50]. This isotope is produced in uranium and plutonium fission and is released into the environment in nuclear weapon tests and by nuclear reprocessing plants.

The beta decay of ^{85}Kr with an endpoint of 687 keV and a half-life of 10.76 years presents a serious background for the dark matter search. Its concentration in the detector can be measured using a second decay mode, $^{85}\mathrm{Kr}(\beta,173\ \mathrm{keV}) \to {}^{85m}\mathrm{Rb}(\gamma,514\ \mathrm{keV}) \to {}^{85}\mathrm{Rb}$, with a 0.454% branching ratio. The lifetime of the intermediate state is 1.46 µs and provides a clear delayed coincidence signature.

For a positive identification, events with two S1 signals and at least one S2 signal are selected, as in some cases the two S2 signals will not be distinguishable. The energy requirements are $20\ \mathrm{keV_{ee}} < \mathrm{S1_1} < 210\ \mathrm{keV_{ee}}$ and $300\ \mathrm{keV_{ee}} < \mathrm{S1_2} < 700\ \mathrm{keV_{ee}}$ for the first and the second S1 peak, respectively, and take into account the energy resolution. The timing condition $0.3\ \mu\mathrm{s} < \Delta t < 5\ \mu\mathrm{s}$ requires a minimum separation because two S1 peaks which are too close in time might not be identified as individual pulses. With these cuts, ^{85}Kr delayed coincidence events are detected with $\sim$30% acceptance, as determined by Monte Carlo simulations, and with virtually no falsely identified events.

Commercial Xe gas contains $^{\mathrm{nat}}$Kr at the ppm level. Most of the gas used in XENON100 was processed by Spectra Gases Co. to reduce the $^{\mathrm{nat}}$Kr content to the $\sim$10 ppb level [51], using their cryogenic distillation plant. During the very first XENON100 run, with a total mass of only 143 kg, a $^{\mathrm{nat}}$Kr level of 7 ppb was measured through the delayed coincidence analysis, consistent with the value provided by Spectra Gases. For the ^{85}Kr-induced background to be subdominant, the fraction of $^{\mathrm{nat}}$Kr in Xe must be about a factor of 100 lower. A $^{\mathrm{nat}}$Kr/Xe ratio of 100 ppt would contribute a rate of $\sim 2 \times 10^{-3}$ evts $\times \mathrm{kg}^{-1} \times \mathrm{keV_{ee}^{-1}} \times \mathrm{day}^{-1}$ from ^{85}Kr [27].

To reduce the Kr in the Xe filling XENON100, a small-scale cryogenic distillation column [52] was procured and integrated into the XENON100 system underground. The column, based on a McCabe–Thiele scheme [53,54], is designed to deliver a factor of 1000 in Kr reduction in a single pass, at a purification speed of 1.8 SLPM (or 0.6 kg/h). A small sample of Xe gas processed with a column of similar design and analyzed by mass spectroscopy, was reported to have a Kr level of 3 ppt [53]. XENON100, however, is the first low background experiment using a large mass of LXe, which is sensitive to a Kr contamination at such ultra-low levels.

A schematic of the XENON100 column is shown in Fig. 10. The Xe gas is cooled using a cryocooler before entering the column at half height. A constant thermal gradient is kept using a heater at the bottom of the column and another cryocooler at the top. Thanks to the different boiling temperatures of Kr (120 K at 1 atm) and Xe (165 K) it is possible to have a Kr-enriched mixture at the top of the column and a Kr-depleted one at the bottom. The Xe with a high Kr concentration is separated by freezing it into a gas bottle, while the Xe at the bottom is used to fill the detector.

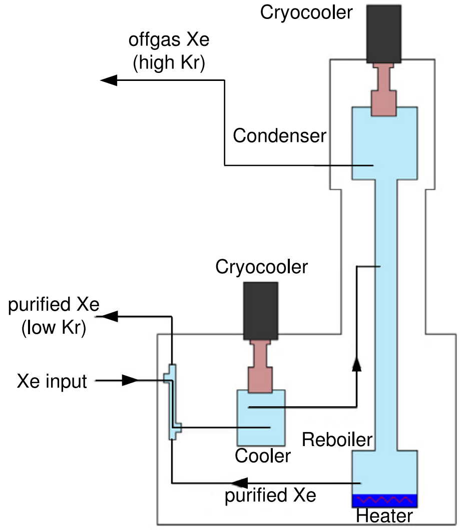

Fig. 10. Schematic layout of the cryogenic distillation column used to separate krypton (including radioactive ^{85}Kr) from xenon. The XENON100 column has a height of about 3 m.

After installation and an initial commissioning run of the new column, a second distillation of the full xenon inventory was performed in Summer 2009. For the commissioning run leading to the first science results [25], the Kr concentration was $\left(143^{+135}_{-90}\right)$ ppt (90% CL), as measured with the delayed coincidence method. This concentration agrees with the value inferred from a comparison of the measured background spectrum with a Monte Carlo simulation [27].

A small leak in the recirculation pump before the first science run [30] led to a Kr increase of a factor $\sim$5. This higher level did not have a large impact on the scientific reach, as demonstrated by the results [30]. In the meantime, a lower Kr concentration, comparable to the one in [25], was achieved by further distillation in late 2010.

3.8. The slow control system and detector stability

A Java-based client-and-server system is used to monitor all relevant XENON100 parameters, such as detector and environmental pressures and temperatures, LXe level, Xe gas recirculation rate, PMT voltages and currents, anode and cathode high voltage, nitrogen purge flow, radon-level in the shield cavity and the environment, cryostat vacuum, etc. The slow control system is constantly monitored by two independent alarm servers located in different countries. These will invoke alarms in case user intervention is required. This system is presented in more detail in [55].

XENON100 shows excellent stability with time. Pressure and temperature, measured every 10 s with high precision, are stable within 0.24% and 0.04%, respectively. Fig. 11 shows the evolution of these parameters for the science data reported in [30], covering a period of $\sim$6 months.

The size of the S2 signal is directly related to the pressure P (in bar) of the Xe gas in the detector [33,56]: An electron extracted into the gas phase by a uniform electric field E (in kV/cm) generates n_{ph} photons,

$$n_{\mathrm{ph}} \propto \left(\frac{E}{P} - 1.0\right) Px, \tag{1}$$

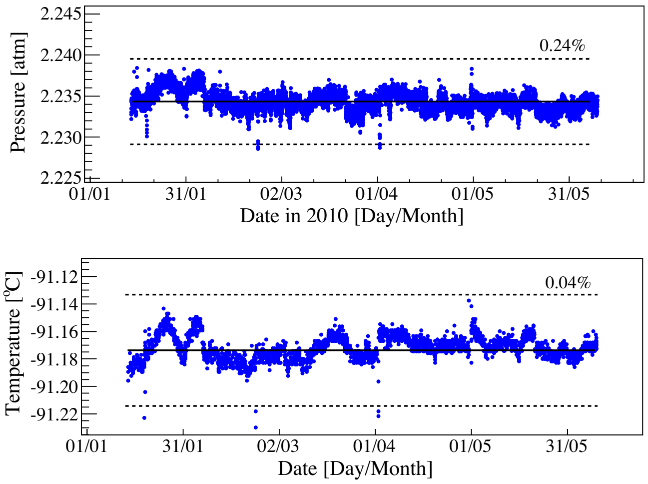

Fig. 11. Long term stability of the Xe gas pressure inside the XENON100 detector (top) and the temperature of the liquid Xe (bottom), measured over a 6 month period. For both parameters, the fluctuations around the average are well within ±0.24% and ±0.04%, respectively.

where x is the gas gap between LXe surface and the anode (in cm). At the XENON100 operating conditions, pressure fluctuations of 0.24% lead to negligible S2 signal fluctuations of <0.05%.

3.9. The data acquisition system

The XENON100 data acquisition (DAQ) system generates the trigger, digitizes the waveforms of the 242 PMTs, and stores the data in an indexed file format. The general DAQ layout is shown in Fig. 12.

The PMT signals are amplified by a factor 10 using commercial Phillips 776 NIM amplifiers and then digitized by CAEN VME V1724 Flash ADCs with 10 ns sampling period, 14 bit resolution, 2.25 V full scale, and 40 MHz bandwidth. At the typical background rate of ~1 Hz, a deadtime-less measurement is possible, since the ADC has a circular buffer with 512 kB memory per channel. An on-board FPGA allows to operate the ADCs in a mode where only parts of the waveform around a peak above a certain threshold are digitized (zero-length-encoding). The position of the peaks within the waveform is stored. For XENON100, this threshold is 4 mV for each channel, corresponding to about 0.3 photoelectrons. Since large parts of an event's waveform consist only of baseline, this leads to a decrease in data size by more than a factor of 10.

For high energy γ-sources, this mode allows calibration rates that are more than one order of magnitude larger than the background rate. The rate is limited to about 30 Hz by the tail of large S2 signals that contains many small peaks exceeding the digitization threshold. For low energy sources, the rate can be higher.

The trigger is generated using the signals of the 68 inner PMTs of the top array plus 16 PMTs from the bottom center, summed with linear Fan-In/Fan-Out modules. It is amplified, integrated ($\tau = 1$ µs), and shaped with a spectroscopy amplifier (ORTEC 450) in order to be able to trigger on very small S2 signals that consist of ~300 PE (corresponding to ~15 ionization electrons), spread within 1 µs. A low threshold discriminator generates the digital trigger signal which is distributed simultaneously to the 31 ADCs. A square-wave voltage pulse of 1 µs width fed into the trigger signal line verified that the trigger threshold was 100% at a pulse height of 24 mV, which corresponds to 150 PE. As not all PMTs of the TPC contribute to the trigger but still detect part of the S2 light, this number has to be corrected by the average fraction of S2 signal seen by the triggering PMTs. It was measured to be 52% of the full S2 signal, leading to a S2 threshold of 290 PE. This number was confirmed by a direct measurement of the trigger threshold: calibration waveforms of 400 µs length were acquired together with the digitized logical trigger signal which was recorded by an unused ADC channel. This allowed for a direct comparison of the spectrum of S2 signals that generated a trigger (identified by the simultaneously stored logical trigger signal) to the full S2 spectrum

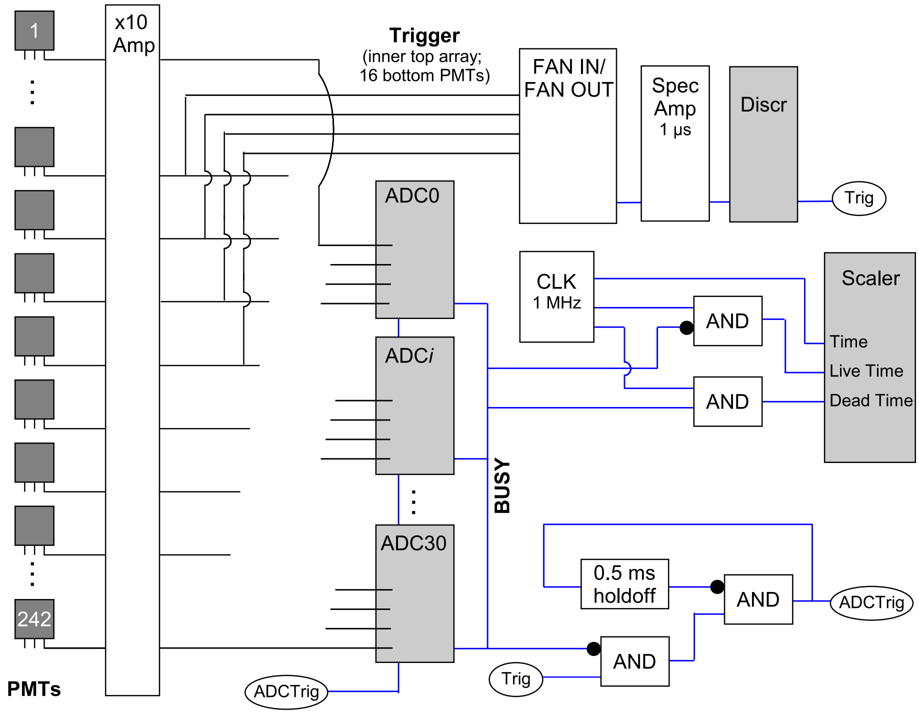

Fig. 12. DAQ schematic of XENON100 for the dark matter search. All 242 PMTs are digitized at 100 MHz sampling rate with Flash ADCs. A hardware trigger is generated using a sum of 68 top and 16 bottom PMTs. The ellipses in the figure indicate connection lines.

(S2 signals without condition on the trigger signal) and to derive the trigger threshold. Additional tests with lowered discriminator thresholds (where many events are noise triggered) also indicate that the trigger threshold is >99% above 300 PE.

The trigger based on the analog sum is used for standard detector operation, however, there is also the possibility to trigger on a majority signal, i.e., when a certain number of PMTs exceeds a threshold. This mode is used for measurements without drift field when no S2 signal is generated and to take data triggering on the active veto. The threshold is higher in this configuration due to the short time coincidence window (10 ns) of the majority signal.

After the science run which lead to the results published in [30], the trigger has been modified in order to lower the threshold. Every ADC generates a 125 mV square-wave output signal for every channel exceeding a pre-defined signal height, which is set to ~0.5 PE and leads to a strong amplification of small signals. The sum of the analog signals is integrated using a spectroscopy amplifier with a time constant of 1 μs and fed into a low threshold discriminator. The improved trigger threshold is >99% above S2 ~150 PE, as derived from a dedicated measurement in which the trigger signal was recorded.

In order not to miss any waveform information, regardless whether the trigger is generated by a S1 or a S2 signal, the trigger is placed in the middle of the event window of 400 μs length, more than twice the maximum electron drift time of 176 μs at 0.53 kV/cm drift field. A 500 μs trigger hold-off is applied after a trigger in order to avoid event overlaps. Additionally, a trigger is blocked when the ADCs are busy or when a high energy veto is applied.

The high energy veto is implemented to reduce the amount of data during calibration at the low energies of interest for the dark matter search. The idea of the veto is to inhibit events which would be triggered by the S1 signal as this is possible only for high energy events. S1 peaks are identified by selecting peaks with a narrow width (to distinguish narrow S1 from wide S2 peaks) by shaping and differentiating the signal in a spectroscopy amplifier. A threshold is then set on the size of the S1 peak and events with a S1 signal above the threshold are rejected. In this case further triggers are inhibited for the next 500 μs in order to prevent triggers generated by subsequent S2 peaks. Because of the S2 amplification these would be even larger than the S1 signal generating the veto.

A VME scaler is used to measure the detector live time and dead time using an external 1 MHz clock and the BUSY outputs of the ADCs. The effect of the trigger holdoff is taken into account separately. The deadtime during science data taking is about 1%.

The time of every accepted trigger is recorded with microsecond resolution. For easier access to the raw waveforms of a particular event, the data are stored in an indexed file format that can be compressed further using standard compression tools during data taking. The extraction of physical parameters from the waveforms is done offline on a computing cluster separated from the DAQ system (see Section 4.2).

4. Low-level analysis

In this section, we focus on how physical quantities are obtained from the raw waveforms recorded by the DAQ system, which can then be used for data analysis.

4.1. PMT gain calibration

The bias voltage for each of the 242 PMTs is set individually and is chosen such that its gain is close to 2.0×10^6 (see Fig. 13). Typical deviations from this gain value are within ±10% and are due to voltage constraints for a given PMT. The gains are determined by stimulating single photoelectron emission from the photocathode using light pulses from a blue LED (λ = 470 nm), driven by a pulse generator. The light is generated outside the detector and fed into the system via two optical fibers, one for the TPC and one for the active xenon veto. Above the diving bell, these two main fibers split into four (six for the veto) in order to distribute the light more uniformly. The light level is chosen such that in <5% of the LED triggers, a PMT shows a photoelectron signal in the time window considered for the analysis. When this is not the case, the window is adjusted in the analysis procedure in order to increase or decrease the photoelectron probability. This procedure allows for the calibration of all 242 PMTs in one run. The light level is sufficiently low to avoid any relevant contamination from two coincident photoelectrons. A pulser frequency of only 100 Hz ensures that the PMT bases are fully charged between two light pulses.

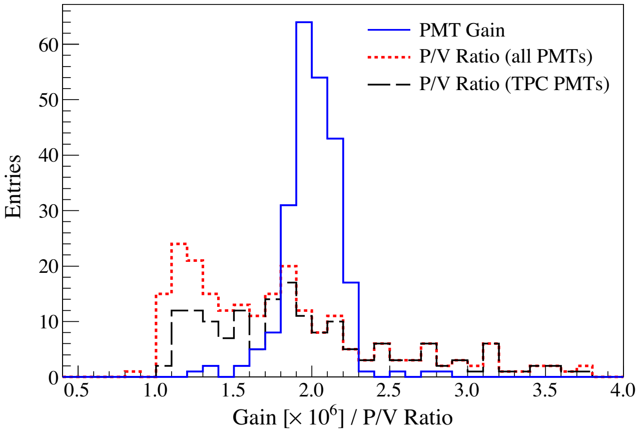

Fig. 13. Distribution of gain and peak-to-valley (P/V) ratio of the PMTs in XENON100. The gain is set to be around 2.0×10^6. Tubes with a better single photoelectron response (higher peak-to-valley ratio) are selected for the TPC.

The position of the single photoelectron peak in the pulse area spectrum (see Fig. 14) is directly proportional to the gain of the tube. It is determined by a simultaneous fit of the single photoelectron peak and the noise peak. The latter is described by a Gaussian function whereas the single photoelectron peak is given by the continuous distribution [48]

$$y(x) = \frac{\mu^x \exp(-\mu)}{\Gamma(x+1)}, \tag{2}$$

where $y(x)$ is the number of counts in the spectrum, μ is the mean of a Poisson distribution, and Γ is the Gamma function. The fit quality

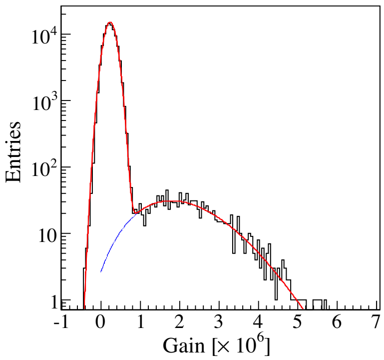

Fig. 14. Single photoelectron spectrum of a typical PMT installed in XENON100. The measured signal (in photoelectrons) has been already converted into the PMT gain. The position of the single photoelectron peak is obtained in a simultaneous fit together with the much higher noise peak close to the origin. This particular PMT has a gain of 2.06×10^6, and a peak-to-valley ratio of 1.54.

is ensured by checking the χ^2-value and by visual inspection of all fits. For monitoring purposes, the individual PMT gains are measured once a week: They show fluctuations within ±2.0% (1σ), in agreement with the overall uncertainty of the gain determination and much lower than the S1 resolution of the detector. The average gain during the science run was stable within ±1%.

4.2. Peak identification

The raw data processor, a ROOT [49] based C++program, is used to derive physical quantities from the waveforms. An event consists of the traces of all 242 PMTs of typically 400 μs length. Since the PMT trace between peaks is not recorded (zero-length-encoding, see Section 3.9), a waveform consists of several digitized subwaveforms together with their respective position in time.

The processing is done in several steps: first, the waveforms are reconstructed from the raw data. The baseline is calculated and subtracted individually for each PMT and for each recorded waveform section. The amplitudes are converted to voltage (see Fig. 15). For the peak finding, the waveforms of the 178 inner PMTs (ignoring 3–4 PMTs that exhibit an increased dark count rate) are summed up. A digital low-pass filter (32 tap filter with a cut-off frequency of 3 MHz) is applied in order to remove high frequencies from the signal to facilitate the determination of the extent of a peak. First, the program searches for S2 peak candidates on the filtered waveform by finding waveform intervals I_{S2} that exceed a threshold of 10 mV for at least 600 ns. In order to be considered as S2 peak candidate, the average signal in the 210 ns before and after I_{S2} has to be lower than 25% of the maximum peak height within I_{S2}. Due to multiple scattering, afterpulses, and small S2 signals from single electrons, an interval I_{S2} might contain several S2 peak candidates. These are identified recursively on the filtered waveform by searching for clear minima close to the baseline between the peaks (bin content below 0.1% of the peak maximum), or for a sign-change in the slope of the waveform. For all peak candidates with a FWHM > 350 ns, parameters such as the position in the waveform, area and width, PMT coincidence level, etc. are calculated. The peak integration is performed over the full extent of the peak as determined above.

The corresponding S1 signal has to be found preceding the S2 signal in time. The much larger S2 signals as well as afterpulsing and S2s from single electrons make an identification of S1 peaks after an S2 signal difficult. Therefore, the algorithm does not attempt to identify S1 signals after the first S2 peak exceeding 300 PE. The S1 peak finder scans the un-filtered sum waveform for peaks exceeding a threshold of 3 mV (~0.33 PE). The waveform regions before and after the peak candidate are taken into account in order to decide whether it is a real peak, and the fluctuations around the baseline are examined in order to reject electronic noise. The detection efficiency for small S1 peaks is very high: >80% for single photoelectrons, >95% for double photoelectrons, and >99% for three photoelectrons. A similar analysis is done on the sum of the active veto PMTs.

For every detected peak candidate, peak properties such as height, width, area, position in the waveform, PMT coincidence level, etc. are determined using the information of all available PMTs. All information is stored for every peak candidate. The identification of valid single-scatter event candidates is done based on these parameters at a later stage in the offline analysis. For example, a valid S1 peak is typically required to be seen on at least two PMTs simultaneously and its width (in ADC samples) must be above a certain threshold in order to reject electronic noise.

The gains of the PMTs are measured and monitored independently (see Section 4.1). Using the gain values for each PMT, averaged over a few months, the peak areas are converted into photoelectrons.

4.3. 3D vertex reconstruction

One advantage of the TPC technique for dark matter searches is the possibility to determine all three coordinates of an interaction vertex in the target volume on an event-by-event basis, as this allows for position-dependent signal corrections and fiducial volume cuts for background suppression.

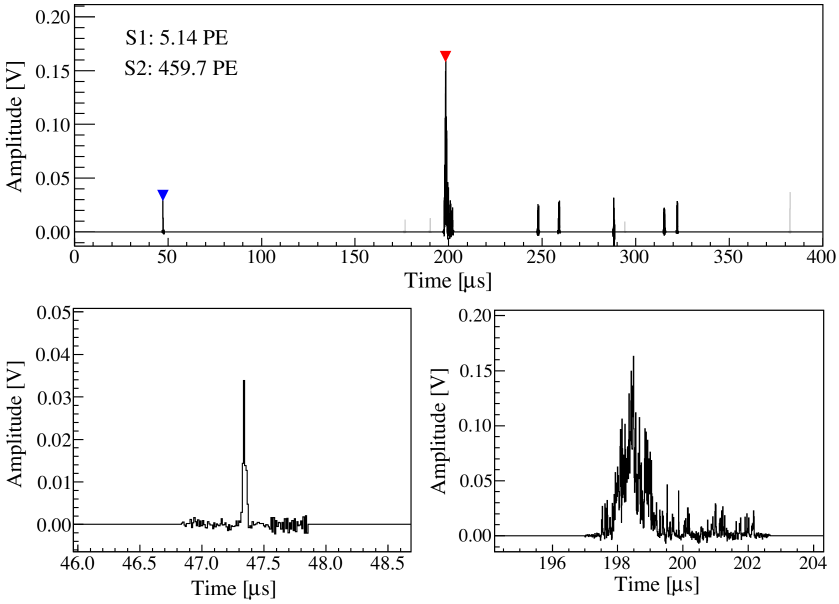

Fig. 15. Example of a low-energy event from background data: The top figure shows the full waveform (400 μs), which is the sum of the 178 PMTs of the TPC. At ~47 μs is the S1 peak (blue marker) of 5.1 photoelectrons (PE), the S2 peak at ~200 μs (red marker) consists of 460 PE. No position-dependent corrections have been applied to these values. The time difference (=drift time) between the peaks is 151 μs. The small structures after the S2 peak are S2 signals from single electrons extracted into the gas phase. With a size of <40 PE they are clearly distinguishable from the main S2 peak. Closer views of the S1 and the S2 peak are shown on the bottom left and right, respectively. (For interpretation of the references to colour in this figure legend, the reader is referred to the web version of this article.)

In a uniform electric drift field, the electron drift velocity is constant (1.73 mm/μs under the present operation conditions) and the z-coordinate is determined from the time difference $\Delta t = t_{S2} - t_{S1}$ between the prompt S1 and the delayed S2 signal. t_{S1} and t_{S2} are determined at the maxima of the pulses. From the maximum drift time and the known TPC length (or via the independently measured drift velocity [34]) this can be converted to the space coordinate z. The z-position resolution of XENON100 is 0.3 mm (1σ) as inferred from events in background data at a well known position near the top liquid layer, the gate grid, or the cathode. Because of the finite width of the S2 signal, two S2 pulses can only be separated if they are more than 3 mm in z apart.

The determination of the (x, y) position exploits that the secondary S2 signal from the charge cloud is generated at a very localized spot right above the liquid–gas interface. This leads to a highly clustered S2 signal on the array of top PMTs, which is detected using the fine granularity of the 1 in. × 1 in. PMTs (see Fig. 16). Three different position reconstruction algorithms have been developed to obtain the (x, y) position from a comparison of the measured top array PMT hit pattern with the one generated by a Monte Carlo simulation. The presence of non-functional PMTs has been taken into account in all algorithms.

The χ^2-algorithm compares the observed PMT hit pattern with the ones from the simulation and finds the (x, y) position by minimizing the χ^2-value. An advantage of this method is that the χ^2 can be used to quantify the quality of the reconstructed position.

Another approach is utilized by the support vector machine algorithm (SVM) [57]: This mathematical procedure is based on training samples from the Monte Carlo simulation, using the signal proportion on each PMT in the top array for a given (x, y) position, to create a base of vectors in a projected multidimensional space. The (x, y) position of an interaction can then be found by solving a sum of scalar products between the vector corresponding to the measured input data and the base vectors defined in the training of the algorithm. The SVM algorithm was used for the analysis presented in Ref. [25].

The third algorithm uses a neural network (NN) [58]: The network consists of units (neurons) with several inputs from other units, and one output whose value is calculated from the inputs. Here, a feed-forward multilayer perceptron is employed. 98 inputs (the PMTs on the top array) lead to the output position vector (x, y). They are connected by one hidden layer with 30 neurons. The network must be trained (backpropagation rule) using Monte Carlo data before it can be used to derive the position corresponding to measured hit patterns. More details can be found in Ref. [18].

All three algorithms give results consistent with each other and with the Monte Carlo simulation for radii $r < 142$ mm. A (x, y) resolution of <3 mm (1σ) was measured with a collimated ^{57}Co source located above the TPC at several r_i while the LXe veto above the diving bell was not filled. This result, shown in Fig. 17, is dominated by the point spread due to the finite size of the collimator opening. The expected resolution based on Monte Carlo data is better than 2 mm. For the science results published in [30], the NN algorithm was used as it shows the most homogeneous response and better agreement with the expectation from a Monte Carlo simulation. The other two algorithms were used to cross check the position obtained with NN and for data quality cuts.

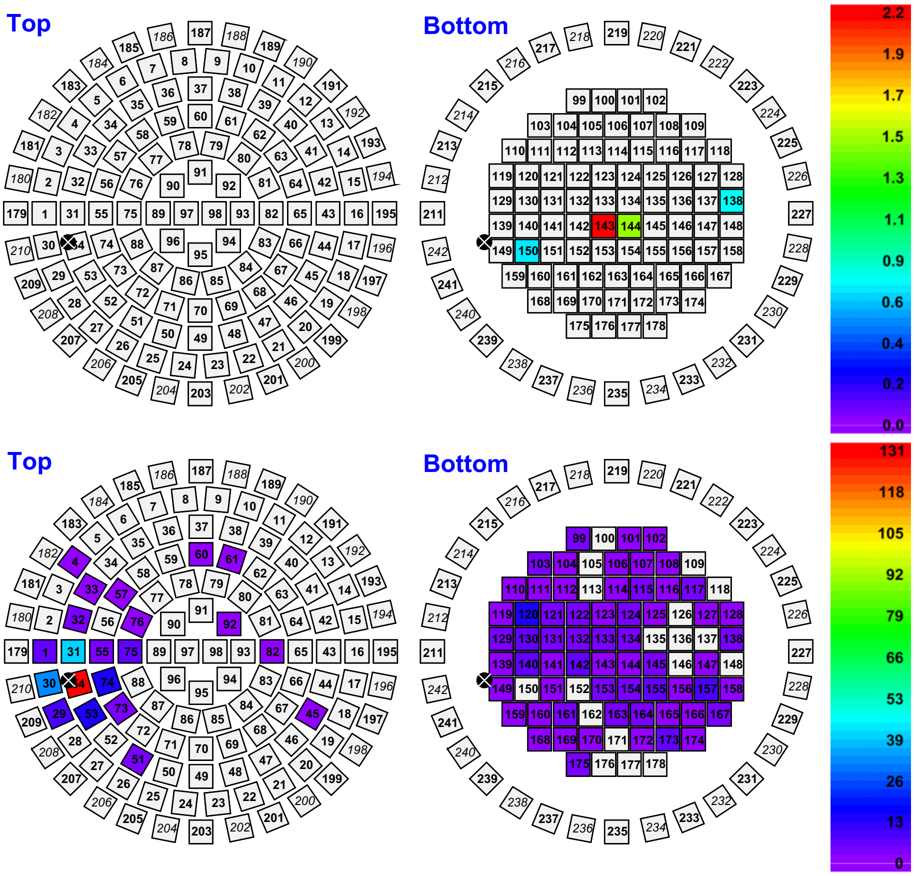

Fig. 16. PMT hit pattern of the event displayed in Fig. 15. Numbers indicate individual PMTs, PMTs 179–242 are in the active veto. The color code is proportional to the signal (in PE) seen by the respective PMT. (Top) S1 hit pattern. Only 4 bottom PMTs see the S1 peak due to the small energy of the event. (Bottom) S2 hit pattern. The hit pattern on the top array (bottom left) is used for the (x, y) position reconstruction. In both figures, the marker indicates the xy-position reconstructed by the neural network algorithm.

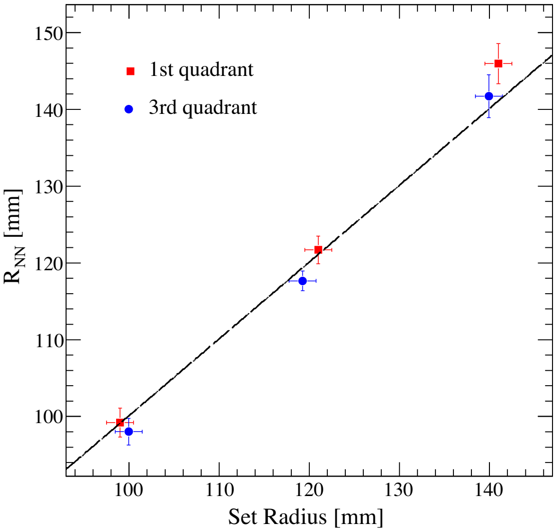

Fig. 17. Set position of the S2 spot from a collimated ^{57}Co source vs. the position reconstructed by the neural network algorithm. The collimator was moved across the detector, hence datapoints exist for the first and the third (*x*, *y*) quadrant. The measurement focused on large radii, where position reconstruction is most crucial because of the fiducial volume cut. Within the uncertainties, set positions and reconstructed positions agree. The diagonal line shows where set and measured radius coincide.

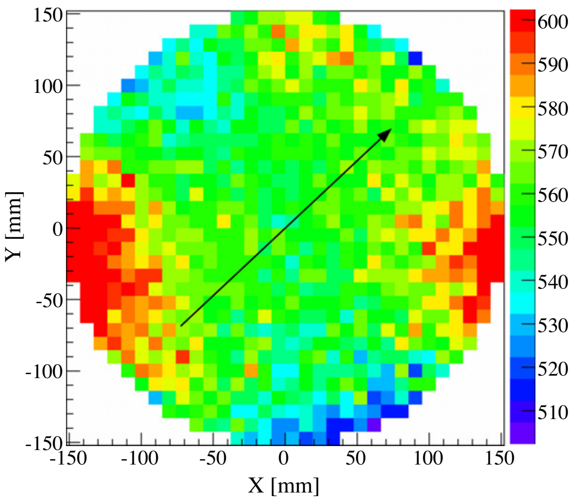

Fig. 18. Measured width Δw (FWHM in ns) of the S2 signal of a backscatter peak in XENON100 background data. Only the topmost layer of LXe is selected. The variation due to warping of the top meshes is maximal at the edges. The arrow gives the maximum overall variation across the whole TPC, which is minimized in the leveling procedure.

5. Detector optimization and characterization

In this section we describe measurements and analyses that have been performed with XENON100 during commissioning in order to characterize the detector response. In particular, we describe the position dependent corrections which are applied to the data.

5.1. Calibration and calibration sources

In order to characterize the detector, calibration sources can be inserted in the XENON100 shield through a copper tube which is wound around the cryostat (see Fig. 5). While vertical source position is restricted to the TPC center, it can be placed at all azimuthal angles.

The sources ^{137}Cs, ^{57}Co, ^{60}Co, and ^{232}Th are used for gamma calibrations. The electronic recoil band in $\log_{10}$(S2/S1) vs. energy space defines the region of background events from β- and γ-particles. It is measured using the low energy Compton tail of high-energy γ-sources such as ^{60}Co and ^{232}Th. The response to single scatter nuclear recoils, which is the expected signature of a WIMP, is measured with an ^{241}AmBe (α,n)-source, shielded by 10 cm of lead in order to suppress the contribution from its high energy gamma rays (4.4 MeV). Besides the definition of the nuclear recoil band and a benchmark WIMP search region, this calibration provides additional gamma lines from inelastic scattering as well as from xenon or fluorine activation at 40 keV (^{129}Xe), 80 keV (^{131}Xe), 110 keV (^{19}F in PTFE), 164 keV (^{131m}Xe), 197 keV (^{19}F), and 236 keV (^{129m}Xe).

5.2. Detector leveling and S2 optimization

Even though the position reconstruction capabilities of the TPC allow to correct for spatial detector anisotropies, it is beneficial to minimize them in the first place. The size of the S2 signal depends on the width *x* of the gas gap between the liquid–gas interface and the anode, see Eq. (1). For an optimal detector response, the detector therefore has to be leveled to get a uniform proportional scintillation S2 signal, and the liquid gas interface has to be adjusted at the optimal height to optimize the S2 resolution. Leveling of the detector within the closed shield was achieved by adjusting set screws in two of the three support legs which can be accessed from the outside of the shield.

For a given calibration peak, the width *w* of the S2 signal (FWHM in ADC samples) is directly proportional to *x*, hence the variation Δw of the S2 width along a line ℓ across the LXe surface was used as a measure for the leveling (see Fig. 18). The leveling was done iteratively using a ^{137}Cs calibration source at several position around the detector. The variation $\Delta w/\ell$ was inferred by fitting a plane to the measured S2 width using only data from the topmost layer of LXe ($\sim$3 mm). It was then reduced accordingly by tilting the detector. After the leveling procedure the value across the line of maximum variation was $\max(\Delta w/\ell) = 0.3$ ns/cm for the remaining S2 variation. It was measured with the dominant backscattering peak in homogeneously distributed background data, again using only the topmost layer of LXe.

These analyses use only basic data selection cuts and do not take into account events close to the borders of the TPC, where S2 width variations from mesh warping are larger. Locally, these effects can cause much larger variations of up to 50 ns. The S2 pulses are additionally widened due to longitudinal dispersion of the electron cloud drifting in the LXe. This is the dominant effect for S2 width variations, leading to widths of $\sim$1 μs for events occurring close to the cathode.

The S2 response was optimized further in the leveled configuration, again using a radially uniform distributed ^{137}Cs source, by varying the overall liquid xenon level until the best resolution of the full absorption S2 peak was found (see Section 5.7). The height of the liquid was monitored with capacitor levelmeters and the best performance was achieved with a LXe level of 2.5 mm above the gate grid.

5.3. Position dependence of the charge signal

After detector leveling (see Section 5.2), two independent effects remain that have an impact on the size of the proportional scintillation signal S2 from the charge: The first is due to absorption of electrons as they drift (finite electron lifetime), leading to a *z*-dependent correction. The second is due to a reduced S2 light collection efficiency at large radii, non-functional PMTs, quantum efficiency differences between neighboring PMTs, as well as non-uniformities in the proportional scintillation gap. This leads to a S2 correction that depends on the (x, y)-position of the S2 signal.

As discussed in Section 3.5, the amount of free electrons generated in an interaction is reduced by absorption on electronegative impurities (mainly oxygen) in the LXe while the electrons are drifted upwards in the drift field. For a given particle energy E, this is described by the exponential relation

$$\mathrm{S2}(E) = \mathrm{S2}_0(E)\exp\left(-\frac{\Delta t}{\tau_e}\right), \tag{3}$$

where S2 is the observed secondary signal and $\mathrm{S2}_0$ is the signal that would have been observed in the absence of drift-time dependent losses. Δt is the drift time, which is the time difference between the prompt S1 and the delayed S2 signal. τ_e is the electron lifetime describing charge losses. Since τ_e is increasing with improved LXe purity (see Fig. 9), it is measured regularly using a ^{137}Cs source, see Fig. 19. As the changes of τ_e with time are small ($\sim$1 µs/day) a calibration measurement once to twice a week is sufficient. Because the τ_e trend shows a linear behavior the data is corrected using a linear fit to all τ_e measurements to reduce the impact of statistical fluctuations.

During the science run leading to the results published in Ref. [30], τ_e was increasing from 230 µs to 380 µs. The drift time correction is largest for events close to the cathode. With $\tau_e > 230$ µs and a maximal drift time of 176 µs, this leads to a maximum correction smaller than a factor 2. In the meantime, even higher τ_e values have been reached as shown in Fig. 19.

The solid angle covered by the PMT arrays decreases for S2 events generated close to the PTFE walls, leading to a lower S2 light collection efficiency and therefore to a smaller observed S2 signal. Other effects such as non-functional PMTs also cause spatial signal variations. The correction due to these effects was determined in the same way as described in Section 5.4 for the S1 light collection efficiency, using ^{137}Cs as well as the 40 keV and 164 keV gamma lines from inelastic neutron scattering and neutron activation, respectively. The corrections obtained from the three lines agree within the uncertainties.

Fig. 20 shows the S2 signal from the 40 keV line as seen by the top and the bottom PMT array, respectively. For all typical fiducial volumes the top PMTs record about 55% of the S2 signal, which is on average ~8600 PE for the 40 keV line summed over all PMTs and after corrections. There is almost no spatial anisotropy on the bottom besides the decrease towards the edge which is due to the decrease in S2 light collection efficiency. The impact of non-working PMTs and mesh warping is irrelevant here since the large distance of >30 cm to the proportional scintillation region spreads the S2 light over the full array. For a fiducial mass of 48 kg ($r < 141$ mm), the maximum correction is about 15% with an RMS of 7.0%. On the top array, spatial S2 variations are larger, which is mostly due to regions of reduced S2 sensitivity where individual PMTs are not working. Locally, this leads to larger corrections. However, the RMS value of 8.8% is only slightly higher than on the bottom array. The signal on both arrays is corrected independently, and only the S2 signal on the bottom array is used for S2/S1 discrimination in the analysis presented in [30].

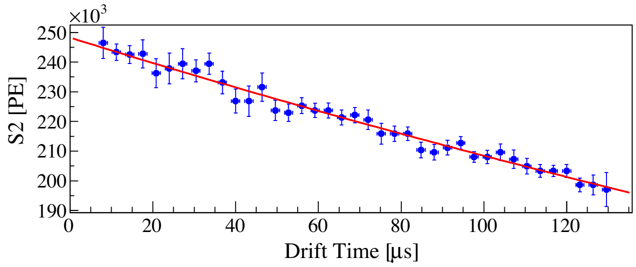

Fig. 19. The charge loss due to impurities in the LXe is determined regularly by measuring the S2 signal of the ^{137}Cs full absorption peak vs. the electron drift time. An exponential fit to the data yields the electron lifetime τ_e, which is 556 µs in this example. The used drift time range is limited to an interval where background and electric field inhomogeneities (Section 5.5) are irrelevant.

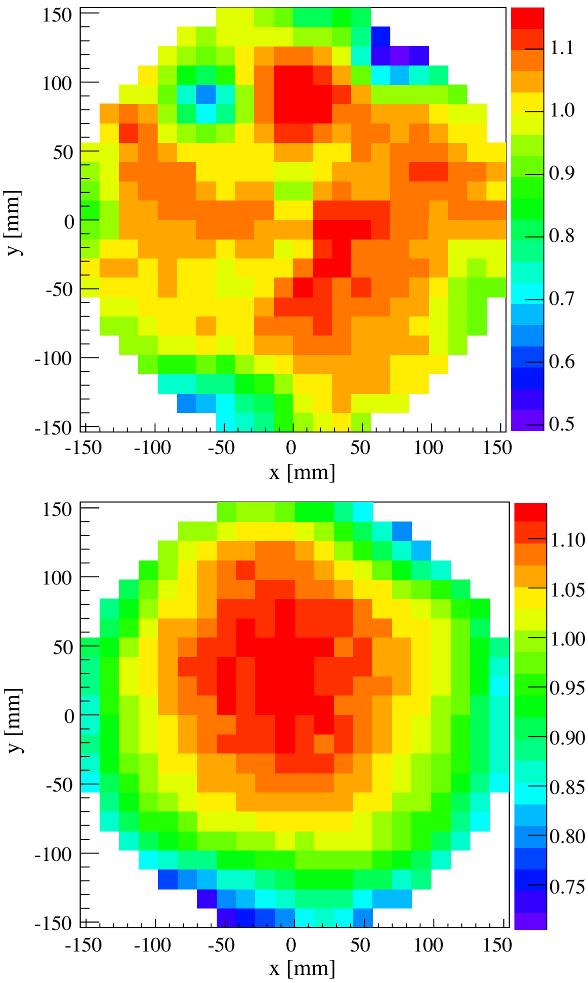

Fig. 20. S2 response of the top and the bottom PMT array, measured with the 40 keV line from inelastic neutron scattering on ^{129}Xe. Shown color-coded is the relative change compared to the mean. The decrease at large radii is due to a reduced S2 light collection efficiency. The top array shows more fluctuations due to non-working PMTs (e.g. at $x \sim -50$ mm, $y \sim 100$ mm).

5.4. Light collection efficiency and light yield

For a given energy deposition, the amount of light that is actually measured by the detector depends on the position of the interaction in the TPC, since solid angle effects, reflectivity, Rayleigh scattering length, transmission of the meshes, etc. affect the light collection of the PMT arrays. Hence, a 3-dimensional map of the light collection efficiency is mandatory to correct the data. A detailed comparison of ^{137}Cs data taken at different positions around the detector confirmed that the TPC response is indeed axial-symmetric as designed. Hence it is sufficient to obtain a (r, z) correction map instead of a (x, y, z) map.

Three different sources were used to infer the correction map: An external ^{137}Cs source (662 keV) taken at three positions around the detector, the 40 keV line from inelastic scattering of neutrons

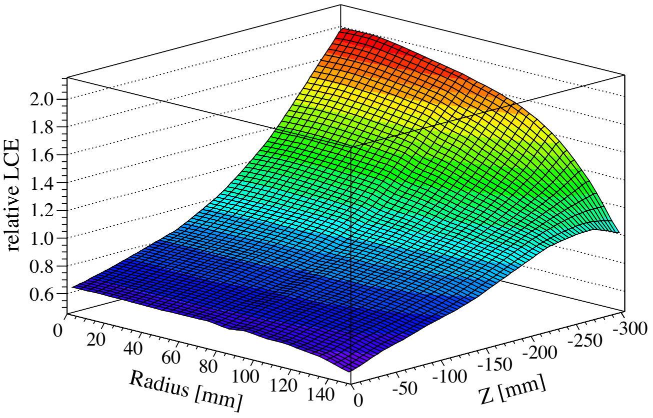

Fig. 21. Correction map for the light collection efficiency (LCE) obtained from the 40 keV line: The vertical axis shows the value to correct a measured S1 (light) signal at a given (*r*, *z*) position. $z = 0$ mm denotes the top of the TPC. The measured S1 signals are divided by the values from this map.

on ^{129}Xe (one source position), and the 164 keV line from neutron-activated ^{131m}Xe with a uniform distribution inside the TPC. For each of the sources, the light yield was determined in (*r*, *z*) bins. The bin size was decreased at larger *r* where the light collection efficiency is expected to fall off stronger while increased statistics from the ^{137}Cs and ^{241}AmBe sources allowed for a finer binning. The light collection efficiency varies by a factor ∼3 across the TPC, with the largest value in the center, right above the bottom PMT array, and the minimum at large *r*, just below the gate grid. The results of the three measurements agree within 3%. The correction map obtained from the 40 keV line, which is used to correct the data, is shown in Fig. 21.

The light yield L_y at 122 keV$_{ee}$ is an important parameter to determine the nuclear recoil equivalent energy scale from the S1 signal (see [59–61] and references therein). However, it cannot be measured directly in large detectors such as XENON100 since gamma rays of this energy do not penetrate into the fiducial volume. Instead, L_y was determined from a fit to the measured volume-averaged scintillation yield for several calibration peaks above and below 122 keV, namely 40 keV (^{129}Xe), 80 keV (^{131}Xe), 164 keV (^{131m}Xe), and 662 keV (^{137}Cs), where all peaks besides the last one are from inelastic neutron interactions from the ^{241}AmBe calibration. An empirical function, linear in $\log_{10}E$, was employed for the interpolation and results in a light yield of $L_y = (2.20 \pm 0.09)$ PE/keV$_{ee}$ at 122 keV and the operating drift field of 0.53 kV/cm (see Fig. 22). Taking into account the measured field quenching [11,62,63], this corresponds to 4.3 PE/keV$_{ee}$ at zero field at 122 keV. The error of L_y includes the uncertainty due to the choice of fit function and takes into account potential variations in the volume-average, as the events from different sources used for the analysis are differently distributed throughout the TPC.

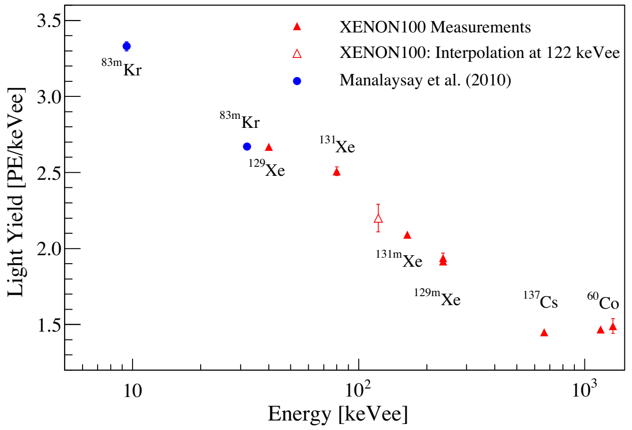

Fig. 22. Measured light yield (in PE/keV$_{ee}$) for different gamma lines used to calibrate XENON100. A direct calibration at 122 keV$_{ee}$ is not possible due to the limited penetration depth of γ-rays of this energy, therefore the value has been interpolated using a fit to the available lines. The values at 9.4 keV$_{ee}$ and 32.1 keV$_{ee}$ are taken from [63] and scaled to the light yield at 122 keV$_{ee}$ and the different electric field. They are given for comparison and not used in the fit.

5.5. Electric field correction

In order to reach the highest possible light collection efficiency and therefore the lowest possible S1 energy threshold, the cathode mesh was optimized in terms of optical transparency using a mesh pitch of ∼5 mm. However, first measurements of the (*r*, *z*) distribution of events in the TPC revealed that the electric field leaking through the cathode was underestimated in the design, leading to an outward bending of the outermost field lines, close to the cathode. There are no charge-insensitive regions from this effect, but it leads to an inwards shift of the reconstructed event radius for $r > 120$ mm and $z < -250$ mm.

In order to optimize the detector response, a field correction was determined by a numerical finite element calculation of the electric field configuration, and cross checked with a simulation using the boundary elements method. The result was verified with three independent measurements: the position of the outermost line of detected events, the electron drift time distribution, as well as the uniform volume density of neutron activated xenon events at 164 keV and 236 keV from metastable states of ^{131}Xe and ^{129}Xe, respectively. A large amount of data with lines from activated xenon was taken following a second ^{241}AmBe calibration at the beginning of 2011, at a reduced extraction field to avoid PMT saturation effects. After applying the field correction, the homogeneity of the event distribution can be confirmed within 2–3% up to $r = 145$ mm, where the precision is limited by the subtraction of the electromagnetic background. This leads to a maximal uncertainty on the field correction which is equal to the position reconstruction uncertainty at the outermost fieldline. It decreases with smaller radii as the correction itself becomes small.

All position-dependent S1 and S2 corrections can be obtained completely independent from the field correction. The field correction, however, improves the detector performance for large fiducial masses and allows a more precise determination of the position of the event vertex for large *r* and *z*. A comparison of this detector region with and without field correction is shown in Fig. 23 for the background data presented in Ref. [25]. As the correction is applied to both calibration and science data, its uncertainty has negligible impact on dark matter results.

5.6. Performance of the active LXe veto

The XENON100 TPC is completely surrounded by a volume of 99 kg LXe with a thickness of ∼4 cm on the side of the PTFE cylinder, below the bottom PMTs, and above the diving bell. Due to the high stopping power of LXe, it effectively suppresses background gamma rays from outer detector materials and the passive shield. In order to improve the background reduction even further, the LXe shield has been equipped with 64 PMTs. 32 PMTs monitor the side of the TPC, whereas two sets of 16 monitor the volume above and below. The shield is optically separated from the target volume and is operated as an active veto. This allows for the rejection of multi-scatter events when both LXe regions show S1 signals within ±20 ns, where the time window is chosen to account for possible ADC bit jitters and the slow component of LXe scintillation.

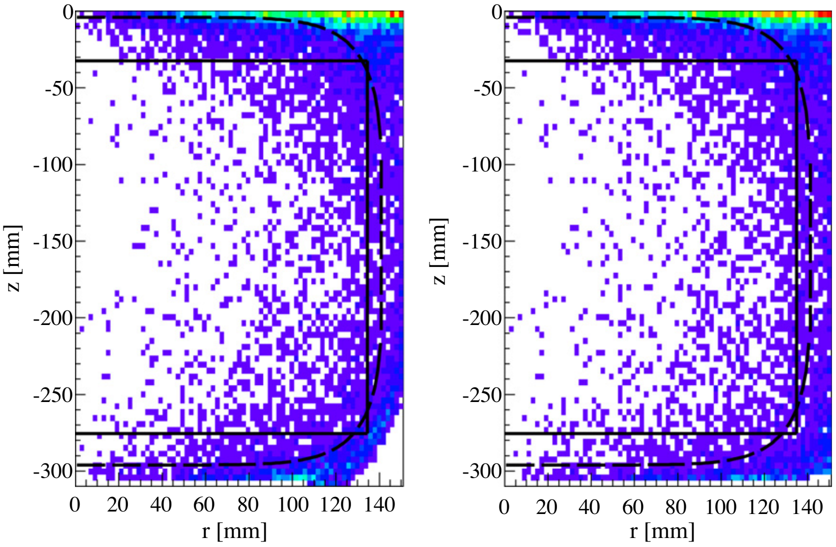

Fig. 23. (r, z) Distribution of background events without (left) and with (right) electric field correction. The non-uniform electric field mostly affects the region at largest r and $|z|$. The solid line indicates the volume of 40 kg fiducial mass used for the analysis presented in [25], the dashed line the 48 kg fiducial mass used in [30].

Due to the limited size of the detector vessel, the position of the PMTs in the veto, and the boundary condition that all support structures and cables for the TPC have to pass through the veto, there is a rather strong position dependence of the veto response. Measurements with a collimated ^{137}Cs source at more than 100 positions all around the detector were performed to determine the veto detection thresholds as function of position. They were estimated from position and width of the measured ^{137}Cs full absorption peak using a Monte Carlo simulation: The 90% detection thresholds are between 180 keV$_{ee}$ and 235 keV$_{ee}$ in the side veto, 130 keV$_{ee}$ below the bottom PMT array, and between 10 keV$_{ee}$ and 30 keV$_{ee}$ above the target volume. The threshold increases to about 450 keV$_{ee}$ in regions behind veto PMTs.

The energy deposition in the veto is slightly anti-correlated to the energy deposition in the TPC and the active veto reduces the single-scatter gamma background in the TPC very efficiently. From a detailed background study [27] using these results, an additional background reduction of 44% and >70% is obtained in the region of interest for the full target and $\leqslant$50 kg fiducial mass, respectively, compared to a passive LXe shield.

5.7. Combined energy scale and energy resolution

Light and charge signal are anti-correlated for interactions in LXe [64–66]. Every calibration line generates an ellipse in the S2–S1 plane, which can be described with a two-dimensional Gaussian in order to determine the anti-correlation angle θ, see Fig. 24. The projection of the peak along this angle allows for an improved energy resolution.

The angle θ has been determined for the 40 keV$_{ee}$ and 80 keV$_{ee}$ peaks from inelastic neutron scattering, for 164 keV$_{ee}$ and 236 keV$_{ee}$ from metastable states of ^{131}Xe and ^{129}Xe, respectively, for the 662 keV$_{ee}$ line from ^{137}Cs, and for the ^{60}Co lines at 1173 keV$_{ee}$ and 1333 keV$_{ee}$. It is quite constant for $E \gtrsim 100$ keV$_{ee}$. The angles for the 40 keV$_{ee}$ and 80 keV$_{ee}$ lines are smaller since the interaction is a combination of a nuclear recoil and a subsequent gamma emission.

From the mean positions and angles obtained from calibration data, the combined energy scale for electronic recoil events has been defined. By comparing the resulting spectrum to Monte Carlo data, it was verified that the combined energy scale is indeed linear. Fig. 25 compares the measured electronic recoil spectrum from the calibration with ^{241}AmBe, using the combined energy scale, with a Monte Carlo generated spectrum. This scale is currently only used for background studies [27]; the WIMP search data is analyzed using a S1-based nuclear recoil energy scale [25,30].

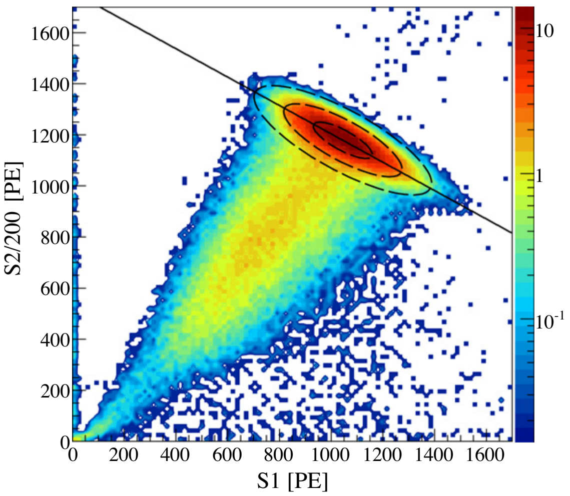

Fig. 24. ^{137}Cs calibration data in position-corrected S2–S1 parameter space. The signals are anti-correlated and a projection along the anti-correlation ellipse leads to an improved energy resolution. The color scale gives the number of events per bin.

The energy resolution has been determined from the same gamma calibration lines for three different energy scales, based on the S1 signal alone, the S2 signal alone, and the combined energy scale, see Fig. 26. All position-dependent corrections have been applied. The energy dependence of the resolution σ/E can in all cases be described by

$$\frac{\sigma(E)}{E} = \frac{c_1}{\sqrt{E}} + c_2, \qquad (4)$$

where E is the gamma energy and the c_i are constants that are different for the three scales. c_2 is compatible with zero for the combined energy scale. At 1 MeV, the resolution is 12.2% for the

S1-based scale, 5.9% for the S2-based scale, and 1.9% in the combined energy scale. The S2-based value is comparable to the resolution of NaI(Tl) crystals and the resolution of the combined energy scale is even better, in particular when compared to large crystals. Fig. 27 shows the change of the ^{137}Cs spectrum using the three scales. For this figure, a veto cut is applied and only events with one interaction in the TPC are considered in order to suppress the Compton continuum.

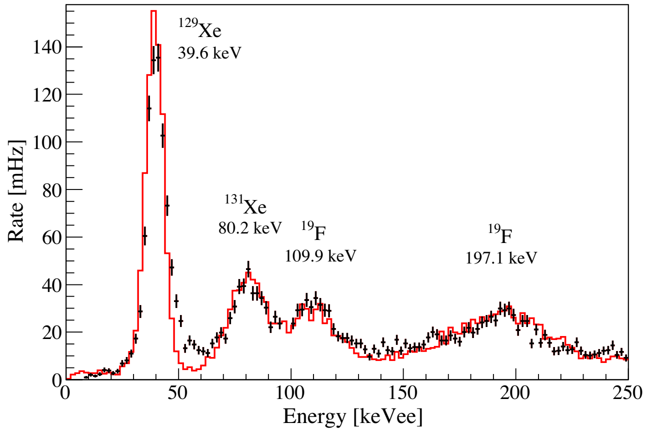

Fig. 25. ^{241}AmBe calibration spectrum in combined energy scale (electronic recoil interactions only). The spectrum agrees very well with the result from a Monte Carlo simulation (red line). (For interpretation of the references to colour in this figure legend, the reader is referred to the web version of this article.)

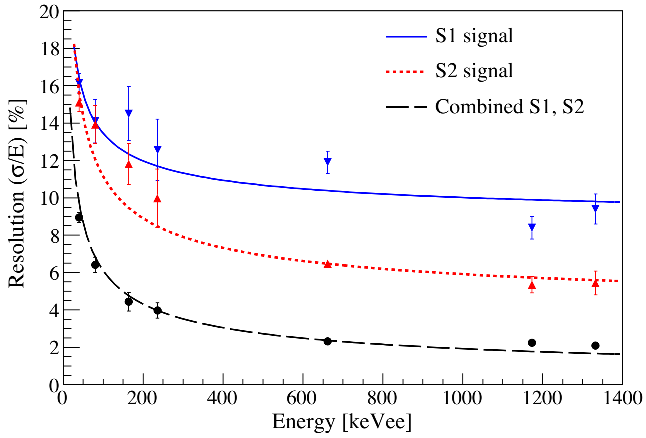

Fig. 26. Measured resolution (σ/E) of gamma calibration lines between 40 keV$_{ee}$ and 1333 keV$_{ee}$ in S1, S2, and combined energy scale, together with fits describing the $1/\sqrt{E}$ dependence.

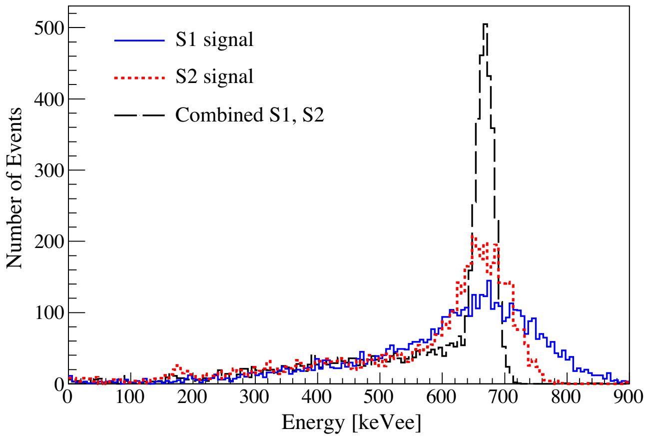

Fig. 27. Spectrum of ^{137}Cs at 662 keV$_{ee}$ in three different energy scales: The resolution (1σ) is 12.5% for the S1 scale, 6.5% for the S2 scale, and 2.3% for the combined energy scale where the anti-correlation between charge and light signal is exploited. Only single-scatter events are considered in the plot and a veto cut is applied, effectively reducing the Compton continuum.

6. Outlook

The XENON100 detector is currently operating in stable conditions underground at LNGS. After providing the most stringent limits on spin-independent WIMP-nucleon scattering cross sections for WIMP masses above ∼10 GeV/c^2 [30], more data are being acquired with improved background conditions and with a lower trigger threshold in order to reach the full sensitivity of the instrument. The next generation instrument, XENON1T, with a total mass of ∼2500 kg of LXe and with 1000 kg in the fiducial target, is already in the technical design phase. XENON100 will be kept operational and running in parallel during the construction phase of XENON1T.

An upgrade of the XENON100 detector is being considered with the goal of increasing the light collection, the operating drift field, and decreasing the overall background by further reduction of the Kr concentration in the LXe. The upgrade could also be useful to test new technologies required for XENON1T.

Acknowledgments

We gratefully acknowledge support from NSF, DOE, SNF, the Volkswagen Foundation, FCT, and STCSM. We are grateful to LNGS for hosting and supporting the XENON program, and especially to the LNGS mechanical workshop for their support during the construction and installation of XENON100. We also acknowledge the support from the LNGS electronics and chemistry workshops, computing department, and engineering team. We would like to thank the many colleagues who have contributed to the XENON100 construction phase, in particular Dr. T. Haruyama.

References

[1] K. Nakamura et al., Particle Data Group, J. Phys. G 37 (2010) 075021. and references therein.
[2] G. Bertone, D. Hooper, J. Silk, Phys. Rep. 405 (2005) 279.
[3] N. Jarosik et al., WMAP Collaboration, Astrophys. J. Suppl. Ser. 192 (2011) 14.
[4] H.C. Cheng et al., Phys. Rev. Lett. 89 (2002) 211301.
[5] A. Birkedal-Hansen, J.G. Wacker, Phys. Rev. G 69 (2004) 065022.
[6] A. Bottino et al., Phys. Rev. D 69 (2004) 037302.
[7] J. Ellis et al., Phys. Rev. D 71 (2005) 095007.
[8] M.W. Goodman, E. Witten, Phys. Rev. D 31 (1985) 3059.
[9] www.lngs.infn.it.
[10] O. Buchmueller et al., Eur. Phys. J. C 71 (2011) 1634.
[11] E. Aprile et al., Phys. Rev. Lett. 97 (2006) 081302.
[12] E. Aprile, T. Doke, Rev. Mod. Phys. 82 (2010) 2053.
[13] E. Aprile et al., IEEE Trans. Nucl. Sci. 51 (2004) 1986.
[14] E.M. Gushchin et al., Sov. Phys. JETP 45 (1979) 5.
[15] E. Aprile et al., Nucl. Instr. Methods Phys. Res. A 556 (2006) 215.
[16] K. Ni et al., Nucl. Instr. Methods Phys. Res. A 551 (2005) 356.
[17] E. Aprile et al., Phys. Rev. D 72 (2005) 072006.
[18] E. Aprile et al., XENON10 Collaboration, Astropart. Phys. 34 (2011) 679.
[19] J. Angle et al., XENON10 Collaboration, Phys. Rev. Lett. 100 (2008) 021303. Updated limit in [59].
[20] J. Angle et al., XENON10 Collaboration, Phys. Rev. Lett. 101 (2008) 091301.
[21] J. Angle et al., XENON10 Collaboration, Phys. Rev. D 80 (2009) 115005.
[22] J. Angle et al., XENON10 Collaboration, Phys. Rev. Lett. 107 (2011) 051301.
[23] G.J. Alner et al., ZEPLIN-II Collaboration, Astropart. Phys. 28 (2007) 287.
[24] V.N. Lebedenko et al., ZEPLIN-III Collaboration, Phys. Rev. Lett. 103 (2009) 151302;
D.Y. Akimov et al., ZEPLIN-III Collaboration. arXiv:1110.4769.
[25] E. Aprile et al., XENON100 Collaboration, Phys. Rev. Lett. 105 (2010) 131302.
[26] E. Aprile et al., XENON100 Collaboration, Phys. Rev. D 84 (2011) 052003.
[27] E. Aprile et al., XENON100 Collaboration, Phys. Rev. D 83 (2011) 082001.

[28] E. Aprile et al., XENON100 Collaboration, Astropart. Phys. 35 (2011) 43.
[29] Z. Ahmed et al., CDMS-II Collaboration, Science 327 (2010) 1619.
[30] E. Aprile et al., XENON100 Collaboration, Phys. Rev. Lett. 107 (2011) 131302.
[31] B.A. Dolgoshein, V.N. Lebedenko, B.U. Rodionov, JETP Lett. 11 (1970) 513.
[32] A.I. Bolozdynya et al., IEEE Trans. Nucl. Sci. 42 (1995) 565.
[33] A.I. Bolozdynya, Nucl. Instr. Methods Phys. Res. Sect. A 422 (1999) 314.
[34] L.S. Miller, S. Howe, W.E. Spear, Phys. Rev. 166 (1968) 871.
[35] M. Yamashita et al., Nucl. Instr. Methods Phys. Res. Sect. A 535 (2004) 692.
[36] V.N. Solotov et al., Nucl. Instr. Methods Phys. Res. Sect. A 516 (2004) 462.
[37] www.cirlex.com.
[38] M. Ambrosio et al., MACRO Collaboration, Phys. Rev. D 52 (1995) 3793.
[39] M. Haffke et al., Nucl. Instr. Methods Phys. Res. Sect. A 643 (2011) 36.
[40] L. Baudis et al., JINST 6 (2011) P08010.
[41] C. Arpesella, Appl. Radiat. Isot. 9/10 (1996) 991.
[42] G. Heusser, M. Laubenstein, H. Neder, in: P.P. Povinec, J.A. Sanchez-Cabeza (Eds.), Radionuclides in the Environment, Elsevier, 2006, p. 495.
[43] T. Haruyama et al., AIP Conf. Proc. 823 (2006) 1695.
[44] A. Baldini et al., MEG Collaboration, Nucl. Instr. Methods Phys. Res. Sect. A 545 (2005) 753.
[45] G. Bakale, U. Sowadaand, W.F. Schmidt, J. Phys. Chem. 80 (1976) 2556.
[46] P.M. Rentzepis, D.C. Douglas, Nature 293 (1981) 165.
[47] N. Ackerman et al., EXO Collaboration, Phys. Rev. Lett. 107 (2011) 212501.
[48] L.C. Alexa et al., Nucl. Instr. Methods Phys. Res. Sect. A 365 (1995) 299.
[49] R. Brun, F. Rademakers (ROOT), Nucl. Instr. Methods Phys. Res. Sect. A 389 (1997) 81–86.
[50] C.Y. Chen et al., Science 286 (1999) 1139.
[51] K. Darabos, private communication, 2007.
[52] http://www.tn-sanso.co.jp/en/.
[53] K. Abe et al., XMASS Collaboration, Astropart. Phys. 31 (2009) 290.
[54] W.L. McCabe, J.C. Smith, Unit Operations of Chemical Engineering, third ed., McGraw-Hill, 1976.
[55] E. Aprile et al., XENON100 Collaboration, to be published.
[56] E.D.C. Freitas et al., Phys. Lett. B (2010) 205.
[57] C.C. Chang, C.J. Lin, LIBSVM: a library for support vector machines. <http://www.csie.ntu.edu.tw/∼cjlin/libsvm>.
[58] A. Zell et al., Stuttgart Neural Network Simulator. <http://www.ra.cs.uni-tuebingen.de/SNNS/>.
[59] E. Aprile et al., Phys. Rev. C 79 (2009) 045807.
[60] A. Manzur et al., Phys. Rev. C 81 (2010) 025808.
[61] G. Plante et al., Phys. Rev. C 84 (2011) 045805.
[62] T. Doke et al., Jpn. J. Appl. Phys. Part 1 41 (2002) 1538.
[63] A. Manalaysay et al., Rev. Sci. Instrum. 81 (2010) 073303.
[64] T. Shutt et al., Nucl. Instr. Methods Phys. Res. Sect. A 579 (2007) 451.
[65] E. Aprile et al., Nucl. Instr. Methods Phys. Res. Sect. B 173 (2007) 113.
[66] E. Aprile et al., Phys. Rev. B 76 (2007) 014115.